Post-fire behaviour of continuous reinforced concrete slabs under different fire conditions

Post-fire behaviour of continuous reinforced concrete slabs under different fire conditions

Yong Wang [a], Yaqiang Jiang [a], Zhaohui Huang [b,*], Lingzhi Li [a,c], Yuner Huang [d], Yajun Zhang [a], Gengyuan Zhang [e], Xiaoyue Zhang [a], Yakun Duan [a]

[a] *State Key Laboratory for Geomechanics & Deep Underground Engineering, China University of Mining & Technology, Xuzhou, Jiangsu, 221116, China;*

[b] *Department of Civil and Environmental Engineering, Brunel University London, Uxbridge, UB8 3PH, UK*

[c] *College of Civil Engineering, Tongji University, 1239 Siping Road, Shanghai 200092, China*

[d] *School of Engineering, The University of Edinburgh, Edinburgh, UK*

[e] *China Academy of Building Research, Beijing 100013, China*

Abstract: An experimental investigation of the performance of reinforced concrete continuous slabs is presented in this paper, following the exposure of the slabs to different compartment fires. The influence that several factors, including compartment fire scenarios, reinforcement ratio, and bar arrangement, have on the deflections, strains, crack patterns, and failure modes is analysed. Results that compared to the uniform fire case, localized or extended punching shear failure modes are more likely to occur in the fire-damaged slabs subjected to the traveling fire due to more cracks. The residual structural stiffness and ultimate loads are enhanced with the increasing reinforcing ratio, but the brittle punching failure readily appeared. Finally, the deflection failure criterion (l/50) and the ACI 318-08 punching shear theory are helpful in predicting the residual ultimate loads of the fire-damaged slabs subjected to any fire scenario.

Keywords: continuous slab; post fire; failure mode; punching shear; ultimate load; theoretical analysis.

[*] Corresponding author, E-mail address: zhaohui.huang@brunel.ac.uk (Z. Huang)

1. Introduction

In recent years, the structural performance of reinforced concrete (RC) slabs in fire has received significant research attention. There have been numerous experimental and numerical studies on the fire performance of RC slabs [1-11]. However, there are limited studies on the residual load capacity of RC slabs to assess the extent of fire damage and reusability [12-14].

So far, the residual responses of isolated simply-supported concrete slabs have been primarily investigated. For instance, Chung et al. [15] investigated the residual strength of fire-damaged RC slabs by means of experimental tests and numerical simulations. However, the test specimens were not loaded during the fire, thus, the load capacities obtained from the test program did not agree with the real conditions of RC slabs in buildings. Wang et al. [16] conducted a test to investigate the residual strength of one full-scale fire-damaged RC two-way slab and proposed the reinforcement strain difference method to predict its load-deflection curve. It was found that the proposed method can be employed to determine the residual strength of post-fire simply supported two-way RC slabs. Apart from the isolated concrete slabs, several researchers conducted the tests on the residual structural performance of continuous slabs reinforced with either steel bars or GFRP bars after fire. For instance, Yu [17] investigated the residual capacity of five two-span continuous concrete slabs (5200 × 1200 × 120 mm) after exposed to fire. As expected, the residual bearing capacity and the initial structural stiffness gradually decreased as the heating time increased. Hou and Zheng [18] and Zheng et al. [19] investigated the post-fire mechanical performance of unbonded prestressed concrete (PC) continuous slabs. It was found that the degradation rate of the load-bearing capacity of PC slabs increased with the increase in heating time and load level. Meanwhile, Hajiloo and Green [12], Gao et al. [20] and Gooranorimi et al. [21] investigated the residual strength of fire-exposed GFRP-RC slabs. Contrary to RC slabs, GFRP-reinforced slabs frequently undergo bond-related failures.

The above review of literature shows that studies on the residual properties of concrete slabs subject to uniform fire have been extensively conducted, but less experimental data is

available on the residual properties of continuous slabs after exposed to different compartment fires. This is an important shortcoming of the available literature data, as different compartment fires frequently occur in modern buildings [22-25]. Thus, Wang et al. [26] investigated the post-fire residual behaviour of five continuous reinforced concrete slabs (named Slabs S1-PF to S5-PF) under various fire scenarios in the spans. The results indicate that the residual material properties of heated compartments and concrete spalling significantly affect the ultimate load and failure mode of the fire-damaged continuous RC slabs. Apart from the flexural failure mode, the punching shear failure also occurred in the fire-damaged continuous slab, particularly in the span with considerable explosive concrete spalling. Note that, the five tested slabs has the same reinforcement arrangement. In addition, about 180 min of fire duration was used in the five tests, including single-compartment, two-compartment and three-compartment fires. In fact, for many fire events, fires were observed to spread from one compartment to another compartment in the same floor or different floors [27]. Thus, the residual behaviour of the continuous slabs subjected to different compartment fires is more representative than the cases where all spans in the continuous slabs are subjected to a uniform fire.

Apart from the experimental studies, the theoretical methods need to be developed to assess the residual strength of the fire-damaged concrete slabs, particularly the residual bearing capacity and failure criteria [26]. At present, several theoretical methods [3, 16, 28-34] were developed to predict the bearing capacity of simply supported two-way concrete slabs at ambient and elevated temperatures. In those developed methods, different flexural failure modes were proposed to predict the bearing capacities of concrete slabs at large deflections (considering tensile membrane action). However, for fire-damaged concrete slabs, another failure mode, such as the punching shear failure, should be considered because of the material strength degradation and the decreased thickness of slabs resulted from concrete spalling [26]. Therefore, the main objectives of this paper are: (1) to investigate experimentally the residual carrying capacity and failure mode of the each span of four three-span full-scale continuous RC slabs under various compartment fire scenarios as well as compare with the observations from other literature; (2) to establish the reasonable failure criteria to determine the residual

ultimate loads of the fire-damaged continuous slabs; (3) to apply the flexural and punching shear theories for evaluating the residual bearing capacity of the slabs and verify their effectiveness.

2. Experimental program

2.1 Design of the specimens

Four three-span RC continuous slabs (named Slabs B1 to B4) were designed according to the specifications of Chinese Standard GB50010-2010 [35]. All slabs were casted using commercial concrete with the characteristic cube strength of 30 MPa at the age of 28 days. The measured concrete cubic strength was 31.5 MPa. The age of the concrete at the time of fire testing was: Slab B1 = 749 days; Slab B2 = 701 days; Slab B3 = 716 days and Slab B4 = 730 days, and the moisture content was 2.3%.

For each slab, hot-rolled reinforcing bars with a diameter of 8 mm were used, and the clear concrete cover was 15 mm. The average yield and ultimate strength of the reinforcing steel were 414 MPa and 475 MPa at ambient temperature, respectively. Figs. 1(a) and 1(b) shows the details of steel reinforcement layouts of the four slabs.

2.2. Test procedure

2.2.1 Fire tests

For the four fire tests, the variables included the reinforcement ratio (spacing: 100 mm or 200 mm), reinforcement layout (discontinuous or continuous on the top reinforcement layout), and different compartment fires. According to Chinese design code [36], the fire resistance of a building is classified as Classes 1 to 4. In fact, to avoid the rapid fire spreading within a building, the fire compartment wall is required. For the fire compartment walls, the required fire resistance times for Classes 1 to 4 buildings are 15 min, 30 min, 45 min and 60 min, respectively. Note that, for the residential building, the fire resistance of the fire compartment wall is at least 30 min. In this case, two time delays (30 min and 60 min) were used to represent the fire spreading from one compartment to another. The fire test durations of four slabs (Slabs B1 to B4) were 360 min, 400 min, 600 min and 600 min, respectively.

During the fire test, each slab was continuous over the interior support (refractory pellet) and was simply-supported on steel rollers at the exterior supports, and each corner was held down by a steel beam. In addition, the uniform distribution load (2.0 kN/m^2) on the top surface of the slab was applied using iron brick.

The locations of three fire compartments A, B, and C are shown in Fig. 1(a). For Slab B1: At 0 min, Compartment B was firstly exposed to fire, and at 60 min, Compartments A and C were simultaneously exposed to fire. At 180 min (235 min), the nozzles in all three Compartments were shut off. For Slab B2: The sequence of the three compartment fires was similar to that of Slab B1, but the time interval between Compartment B and Compartments A and C was 30 min. For Slab B3: Compartments A, B, C were sequentially exposed to fire, and time delay was 60 min. For Slab B4: Compartments A, C, B were sequentially exposed to fire, and the time interval and the fire duration of each compartment were 60 min and 180 min, respectively. Note that, for each compartment, its heating time was about 180 min. Locations of thermocouples are indicated in Figs. 1(c) and 1(d), and other details of four fire tests can be found in Ref. [27].

2.2.2 Residual tests

After the fire tests all four slabs were moved from the furnace and stored in the structural lab for approximately 3 months. Then the fire-damaged slabs were tested on the new test rig, as shown in Fig. 2. For the residual tests, the fire-damaged slabs were renamed as Slabs B1-PF to B4-PF for Slabs B1 to B4.

(1) *Loading apparatus*

As shown in Figs. 2(a)-2(b), based on the Standard of Concrete Testing Method of China [37], the slab's edges were simply supported by steel rollers on the wall, and the load was applied to the slab using two jacks. There were no horizontal restraints provided along the edges of the slab.

For the residual tests, the loading was applied proportionally on the three spans. Before the load reached 150 kN, at each loading step, the load increment on each span was 30 kN. In other words, the load increment on Jack J1 was 30 kN, and that on Jack J2 was 60 kN. The

140 load on each compartment applied by Jack J2 can be obtained according to the corresponding
141 pressure transducer (see Fig. 2(c)). After the load reached 150 kN, the load increment on each
142 span was 10 kN. The applied load at each loading step was kept for 5 min.
143 As indicated in Fig. 2(c), each corner of the slab was held down by a steel beam. The reaction
144 forces at the corners were measured by four pressure transducers (Points P-1 to P-4). The
145 failure of a slab was governed by: 1) conventional mid-span deflection failure criterion; 2)
146 concrete crushing on the top surface; and 3) punching shear failure. Once any one of those
147 failure conditions was reached, the test was terminated.
148 (2) *Strain measurement*
149 Concrete strain gauges (such as Points A-C-1 and A-C-2) were placed on the top surface of
150 the slabs, as shown in Fig. 3(a). To reduce the damage of the test slabs, only four bottom
151 reinforcement strain gauges (such as Points A-S-1 to A-S-4) were arranged in each span of
152 the slabs.
153 (3) *Deflection measurement*
154 Fig. 3(b) shows the positions of the vertical and horizontal displacement transducers. Three
155 LVDTs (Points V-A, V-B, and V-C) were placed to measure the mid-span vertical deflections
156 of the slab, while its horizontal deflections were measured by two LVDTs (Points H-1 and H-
157 2).

158 ***3. Fire test results***

159 Figs. 4 and 5 show the average furnace temperature, concrete and steel temperature-time
160 curves of four slabs during the fire test. Table 1 gives the maximum temperatures of each
161 compartment, concrete (top and bottom surfaces) and steel (bottom and top steel) at various
162 locations in Slabs B1 to B4. As indicated in Fig. 1(d), for concrete, each thermocouple tree
163 consisted of six thermocouples (such as AT-1 to AT-6) and for steel reinforcement, there were
164 four thermocouples (such as R-1 to R-4).
165 As indicated in the Table 1, the maximum temperatures for the bottom concrete (steel) ranged
166 from 671 (529) °C to 1130 (718) °C, with an average value of 893 (645) °C. The residual
167 strength of the bottom concrete and the bond between concrete and steel were seriously

damaged due to the higher temperatures. In contrast, the top concrete and the bond between concrete and steel had higher residual strengths due to the lower maximum experienced temperature (average value: 246 °C and 345 °C). As discussed in Ref. [26], the average concrete (steel) temperatures on the bottom and top surfaces of the heated spans were 828 (781) °C and 254 (497) °C, respectively. Note that, as indicated in Fig.4, the maximum temperatures near to top surface of each span reached after the time of maximum gas temperature. The delayed failure (structural integrity) of each span occurred during the cooling phase, although the most spans exhibited integrity during the heating phase. In fact, as discussed in Refs. [38-39], more attentions should be brought to the structural behaviour during the cooling phase, and thus the duration of heating phase (DHP), was proposed to assess the burnout resistance of the member throughout a given fire exposure.

Similar to the observations in Ref. [26], severe post-cooling spallings (with the concrete falling into pieces) occurred prior to the residual test due to the moisture absorbed by the calcareous aggregate (rehydration). Compared to thermal-hygral or thermal-mechanical spalling [40], the post-cooling spalling was much slower, but it continued up to the beginning of the residual test (approximately 2 months). This post-cooling spalling should be considered in the repair, since the bottom weak concrete layer will seriously affect the bond strength between concrete and steel. In addition, it can been seen from Table 1 that the residual deflections of each span for Slabs B1 to B4 at the end of the fire test were relatively small. However, for the large deformed slab during fire test the residual performance of that slab may be different compared to the the present slabs due to various permanent and irrecoverable strains, such as the plastic and transient creep strains [38-39].

4. Post-fire mechanical tests

This section discusses the residual behaviour of each slab and a brief explanation of the observed behaviours, including the new cracks, failure mode, load-deflection curves, reaction forces at the corners, and the concrete and steel strains.

4.1 Failure behaviour

Figs. 6–9 show the crack pattern and spalling on the top and bottom surfaces of each span in

196 the four slabs. For each fire-damaged slab, the red and dark lines indicate new and original
197 cracks which were formed during the fire test, respectively.

198 ***4.1.1 Crack patterns***

199 - Slab B1-PF

200 Figs. 6(a) and (b) show the crack pattern on the top surface of slab B1-PF (steel spacing: 200
201 mm). During the residual test, before the loading reached 120 kN, small new cracks appeared
202 on the top surface, and the original cracks gradually widened with increasing loads. After 120
203 kN, large new arc cracks appeared near the four corners of each span. Due to the higher strain
204 on the concrete corners (2672 με), the concrete crushing occurred on the top surface of Span
205 A. In addition, for Span B, one circular punching cone (red circle) formed in the middle region,
206 indicating that the shear punching failure (shear-compression crush: a combination effect of
207 both shear and compression forces) occurred in this span. However, for Span C, only arc
208 cracks appeared on the top surface, and no brittle failure occurred.
209 Figs. 6(c) and (d) show the crack pattern on the bottom surface of Slab B1-PF. Clearly, there
210 were two kinds of failure modes, i.e., the flexural failure mode (Spans A and C) and the
211 overall punching failure mode (Span B). For Spans A and C, the flexural cracks extended
212 from the centre to the edges, while the shear punching area appeared at the centre of Span B.
213 The main reason is that there were numerous original cross cracks (+ shape) on the top surface
214 of Span B, and fewer cross cracks appeared on the two edge spans. The original cross cracks
215 appeared owing to the upward deflections (or negative moments) of Span B during the fire
216 [27], and the crack spacing basically coincided with the steel spacing (200 mm) [16, 41].
217 Clearly, these cracks led to a serious degradation of the structural integrity, decreased bond,
218 and the stress (strain) concentration. For instance, as discussed later, the steel at three points
219 of Span B suddenly exceeded 10000 με at approximately 160 kN, indicating that a brittle
220 failure and strain concentration occurred. The comparison implies that the original cracks that
221 occurred during the fire test had important effects on the failure modes of the fire-damaged
222 slabs.

223 - Slab B2-PF

Figs. 7(a) and (b) show the crack patterns on the top surface of Slab B2-PF (steel spacing: 200 mm). During the residual test, before the loading reached 60 kN, many small arc cracks appeared on the top surface of Spans A and C. As the load increased, the arc cracks gradually widened. At approximately 210 kN, a punching shear failure of Span C occurred with one hole. Furthermore, the concrete crushing (maximum concrete strain: 3386 με) on the top surface of Span A suddenly occurred as well as the steel yielding (reinforcement strain: exceeded 10000 με), as discussed later. Thus, compared to Slab B1-PF, the structural stiffness of Slab B2-PF was larger, owing to the shorter fire duration and fewer original cross cracks (smaller fire time delay, i.e., 30 min). This observation also implies that the fire scenarios have important effects on the failure mode of the middle span in the fire-damaged slab, as they can lead to different cracks or spalling during the heating stage [27].

Figs. 7(c) and (d) show the crack pattern on the bottom surface of Slab B2-PF. Clearly, compared to Span B, serious flexural-punching shear failure occurred in Spans A and C due to higher experienced temperatures (see Table 1) and lower boundary restraint, particularly on Span C.

Hence, the failure mode of each span in one continuous slab was primarily dependent on the experienced maximum temperatures, fire duration, equivalent reduction factor of the strength across the section, and original crack distribution. In addition, the comparison between Slabs B1-PF and B2-PF indicates that the time delays (30 min and 60 min) have an important effect on the failure mode of the initially heated span of the continuous slab. As the time delay increased, the possibility of punching shear failure increased, e.g. Span B1-PF-B.

- Slabs B3-PF and B4-PF

Figs. 8(a) and (b) show the crack pattern on the top surface of Slab B3-PF (steel spacing: 100 mm). Due to many small original cracks in Spans B and C, punching shear failure occurred with four holes on the top surface and smaller vertical deflections. These punching shear areas appeared around the loading plate on the top surface.

More importantly, in contrast to Slabs B1-PF and B2-PF, a large amount of concrete (area: 2.5 m^2) fell from the bottom surface of two spans in Slab B3-PF (Figs. 8(c) and (d)), particularly near the interior supports. The main reason for this is that higher reinforcement

ratio led to more small and tiny original cracks [27], indicating that the bond between the concrete and steel was seriously compromised. In addition, owing to fewer original cracks in Span A, the flexural failure modes occurred, such as new corner and arc cracks. Thus, the failure mode indicated that the fire-damaged slabs with higher reinforcement ratios had a higher residual bearing capacity, but the punching shear failure easily occurred because of numerous small original cracks (negative moment). Compared to Slabs B1-PF and B2-PF, the original crack width on the top surface of Slab B3-PF was much smaller due to the smaller steel spacing (100 mm). The comparison indicates that the residual property of the steel has a large effect on the flexural carrying capacities; however, the residual property of the concrete, original crack patterns (particularly crack spacing), and load type (concentrated load) have a greater effect on the failure mode.

Figs. 9(a) and (b) show the crack pattern on the top surface of Slab B4-PF (steel spacing: 200 mm). In contrast to the flexural failure (arc and flexural cracks) of Spans A and B, the punching shear failure of Span C occurred. In addition, like Slabs S1-PF and S2-PF, the bottom concrete in Slab B4-PF did not fall off, as shown in Figs. 9(c) and (d). However, due to the negative reinforcement layout, the bearing capacity (120 kN) of Slab B4-PF was the smallest. The comparison further indicates that the reinforcement ratio and reinforcement layout have a significant effect on the bearing capacity of the fire-damaged slabs. Hence, the beneficial or detrimental effects of the reinforcement ratio (layout) should be considered in the residual property judgement of post-fire continuous slabs.

4.1.2 Failure criteria

Table 2 shows the bearing capacity (P_u) and ultimate deflection of each span (δ_u) in the four slabs at the end of the residual test. Note that, the post-fire failure of the slab is assumed to occur when [37]: (1) The concrete crushing occurs on the top surface of one span. (2) The mid-span deflection of one span exceeds $l/50$, l is the length of the shorter span. (3) The punching inside or outside the shear zone occurs in any span.

To be conservative, the smallest load of three spans can be considered as the bearing capacity of the slabs. Thus, the bearing capacities of Slabs B1-PF to B4-PF were 145.3 kN, 190.4 kN,

229.1 kN, and 120.0 kN, respectively.

As shown in Table 2, for one span with yield failure, the ultimate deflections ranged from 26.9 mm to 51.1 mm, with an average deflection of 37.5 mm. In addition, for the spans with punching shear failure, the ultimate deflections ranged from 14.9 mm to 34.5 mm, with the average ultimate deflection of 25.3 mm. Thus, for a post-fire slab with any failure, the deflection failure criterion $l/50$ (about 29 mm) is suitable for determining the residual bearing capacity of the span. This observation is similar to the conclusion in Ref. [26].

In fact, the conventional reinforcement strain (such as 0.01) is often used to determine the bearing capacity of unheated slabs [35]. However, this is not suitable for determining the bearing capacity of the heated slabs. For instance, for many spans, the reinforcement strains at lower load levels exceeded 10000 με due to the combination of several factors, including load concentration, cover falling, decreased steel properties and bond degradation. As discussed later, a larger value of steel failure strain (0.02) may be more reasonable.

4.1.3 Discussions

According to the observation in Ref. [26] and the present slabs, it can be concluded that compared to Slabs S1-PF to S5-PF (exposed to uniform fire), the punching shear failure or the flexural-punching combined failure easily appeared in the present slabs subjected to traveling fire. For instance, only four spans in Slabs S1-PF to S5-PF (total 15 spans) had the punching shear failure, but six spans in Slabs B1-PF to B4-PF (total 12 spans) showed this failure behaviour. One reason is the longer fire duration of the present tested slabs. Another reason is that more cross shape (+) original cracks and long-span cracks appeared on the top surface of Slabs B1 to B4 due to the complex deflection trend (upward and downward deflection) of each span [27]. No doubt, this cracking pattern led to the lower structural integrity of the fire-damaged slab and thus its flexural behaviour cannot sufficiently develop. On the other hand, for Slabs S1-PF to S5-PF [26], many short-span original cracks mainly appeared near to the internal supports, and thus the failure at internal support (larger cracks on the top surface) easily appeared during their residual tests. However, for the present tested slabs, less failure at internal support appeared and larger cracks mainly appeared on the

middle region of each span.

In all, the above comparison indicates that the fire scenarios (uniform and travelling fire) have important effect on the failure mode of the fire-damaged continuous slabs, since they led to different original cracking distribution of the slabs during the fire test. In other words, for the uniform fire case, the slab over internal supports may be the weakest region of the continuous slab. For the travelling fire case, the mid-span region of each span may be the weakest region of the slab. No doubt, this observation should be further verified by more residual strength tests of the continuous slabs.

Note that, because of the concentrated loads, punching shear failure at the loading location is a recurring event. Thus, the loading system considerably influences the failure mode of the fire-damaged slabs, and the present observation may not suitable for the uniform load case. However, the present loading case can be considered as the worst case. In fact, for most practical design cases, the brittle punching shear is undesirable, the yield mechanism cannot develop before punching. Thus, one traveling fire scenario which easily leads to the punching shear failure of the fire-damaged slab, particularly near to the support, can be considered as the worst fire scenario. In addition, for the post-fire rehabilitation and resilience, the reasonable strengthening technique should be used to change the mode of failure from punching shear failure to a pure flexural failure [42-44], including the cementitious materials (ECC or epoxy matrix), installation method (prefabricated or cast-in-place), reinforcement type (FRP, reinforcing bar and steel plate).

4.2 Deflection and corner forces

This section discusses the vertical and horizontal deflections of each slab as well as the reaction forces at the corners. For the vertical deflection, positive (negative) displacement is downward (upward); while for the horizontal deflection, positive (negative) displacement indicates outward (inward) movement.

4.2.1 Load-mid-span vertical deflection response

Figs. 10(a)–(d) show the load-deflection curves of the fire-damaged Slabs B1-PF to B4-PF. In addition, the initial residual structural stiffness (K_0), the residual bearing capacities (P_u),

energy ductility (μ_E) and the ultimate deflections (δ_u) are briefly discussed, as indicated in Table 2. Note that, the initial structural stiffness K_0 of each span is the ratio between P_e and its corresponding mid-span deflection (δ_e), and P_e and δ_e values of each span can be obtained according to the significant variation in the slope of the load-deflection curves.

- **Initial residual structural stiffness**

As shown in Table 2, for the four fire-damaged slabs, the average K_0 of the middle and edge spans were 8.6 and 15.3 kN/m, respectively. This is similar to the average values (13.03 kN/m) of the heated spans in Ref. [26]. However, for Slabs S1-PF to S5-PF, there are larger difference among K_0 due to different number and position of the heated spans. For the present slabs, the difference in the initial structural stiffness between the middle span and the edge span can be neglected, as indicated in Table 2. Thus, the beneficial effect of the boundary restraint can be neglected in the residual serviceability assessment, particularly for exposed to travelling fire case.

- **Energy absorption**

The energy ductility (μ_E) was used to assess the ductility, as shown in Table 2 and Fig. 11. The energy ductility (μ_E) is ($E_{total}/(2E_{el}) + 0.5$), where E_{total} and E_{el} are the elastic and total energies (areas of the load-deflection curve) of the fire-damaged slab [20, 26], respectively. As shown in Table 2, the μ_E value of the heated middle (edge) spans ranged from 1.06 (1.26) kN mm to 1.90 (4.80) kN mm, with the average value of 1.32 (2.55) kN mm. Note that, this observation is different from those of the concrete slabs (thickness: 80 mm) subjected to uniform fire [26]. For instance, the μ_E value in Ref. [26] of the heated middle (edge) spans ranged from 9.99 (1.58) kN mm to 19.91 (6.28) kN mm, with the average value of 13.38 (3.22) kN mm. On one hand, μ_E of the present slabs (thickness: 100 mm) were smaller than those of the tested slabs in Ref. [26]. As the depth increased, the ductility was decreased. On the other hand, there were smaller fluctuations in the μ_E values of the present concrete slabs, particularly in those of the middle spans, indicating that the effect of the boundary restraint on μ_E decreased. Thus, compared to uniform fire scenario, the traveling fire scenario tends to decrease the residual structural ductility of the concrete slab due to more complex cross cracks and longer fire duration. In all, the effect of the fire scenario (uniform or traveling) on the

residual structural behaviour should be considered in the post-fire performance assessment or repair design.

- **Bearing capacity**

For each slab, the minimum ultimate load within the three spans was considered as the actual ultimate load of the slab. Thus, the bearing capacity of Slabs B1-PF to B4-PF were 145.3 kN, 190.4 kN, 229.1 kN, and 120.0 kN, respectively, with an average value of 171.2 kN. Due to larger thickness (100 mm), the ultimate load of the present tested slabs were relatively higher than those (average value: 126.8 kN) of Slabs S1-PF to S5-PF (thickness: 80 mm) [26]. In addition, compared to the other three fire-damaged slabs, the bearing capacity of Slab B4-PF was the minimum due to the smaller reinforcement ratio, discontinuous top reinforcement layout, and longer fire duration. Thus, continuous reinforcement layouts and higher reinforcement ratios are beneficial to enhance the residual carrying capacities of the slabs (Slab B3-PF), particularly the flexural capacities, as the flexural strength is mainly dependent on the reinforcement strength and concrete compressive strength on the top surface [45-46]. It can be seen that for any fire scenario, increasing thickness and reinforcement ratio are the most effective methods to enhance the residual capacities of the continuous slabs. However, the possibility of punching shear (brittle or sudden) failure increases with increasing reinforcement ratio due to the smaller crack spacing.

Overall, for any fire scenario, the ultimate load of one span in the fire-damaged continuous slab was primarily dependent on the reinforcement ratio and layout, original crack distribution, cover falling, and boundary conditions. Increasing the reinforcement ratio, providing a continuous reinforcement layout, increasing the original crack spacing and strengthening the cover will be beneficial to enhancing the residual strength of the fire-damaged slabs. In addition, different compartment fires (different fire directions or time delays) that lead to more original cracks and serious concrete spalling in one span will result in a decreased residual strength or brittle failure, particularly in the middle span.

4.2.2 Horizontal deflection and reaction forces

Fig. 12(a) shows the measured horizontal deflection-load curve of Slabs B1-PF and B2-PF.

394 The horizontal deflection is the horizontal component of the corresponding local
395 displacement. During the early stage, the horizontal deflection of each measured point was
396 small due to the small vertical deflection. As the load increased, the horizontal deflection
397 rapidly increased until the end of the test, particularly for Point H-2. In addition, the load-
398 deflection trends differed between Points B1-PF-H-1 (B2-PF-H-1) and B1-PF-H-2 (B2-PF-
399 H-2). However, compared to the maximum vertical deflections, the maximum horizontal
400 deflection (approximately 3 mm) of each post-fire slab was smaller. In all, the deflection trend
401 and the maximum horizontal deflection were similar to the observation in Ref. [26].
402 Figs. 12(b)-(c) show the reaction forces measured by pressure sensors P-1 to P-4 of Slabs B1-
403 PF and B3-PF. On the one hand, similar to the results in Ref. [26], the reaction forces at each
404 measured point gradually increased with increasing loads, and the maximum values were 11.0
405 kN and 14.0 kN, respectively. On the other hand, at the end of each test, the average reaction
406 forces at the four points were 8.1 kN and 10.1 kN, respectively. It can be seen that the fire
407 scenario has little effect on the residual horizontal deflection and the reaction forces of the
408 fire-damaged continuous slabs.

409 ***4.3 Concrete and reinforcement strains***

410 The measured concrete and reinforcement strains for the slabs are shown in Figs. 13(a)–(d),
411 and the concrete peak strain and steel yield strain are given according to Ref. [45]. A positive
412 value represents a tension strain while a negative value indicates a compressive strain. The
413 strains at some measured points are not shown, owing to the malfunction of the strain gauges.
414 As shown in Figs. 13(a)-(d), during the early stage, the concrete strain at each point was small.
415 Then, the concrete compressive strain at each corner quickly increased with the load until the
416 end of the test. In addition, in some cases, concrete crushing occurred during the test, such as
417 with Spans B1-PF-A and B2-PF-A, and the measured concrete strains nearly reached the peak
418 strains. However, for the punching shear failure mode, the measured concrete strain was
419 smaller, such as with Span B3-PF-C. For instance, the average maximum concrete strains
420 were 2409×10^{-6} (Span B1-PF-A: 180 kN), 2701×10^{-6} (Span B2-PF-A: 209 kN) and $671 \times$
421 10^{-6} (Span B3-PF-C: 227 kN), respectively. Thus, similar to the observation in Ref. [26], the

corner concrete strain can reflect the failure mode of the post-fire continuous slab.

As indicated in Figs. 13(a)–(d), the reinforcement strains in most of the measured points gradually increased with the loads; however, similar to the reinforcement strain development in Slabs S1-PF to S5-PF [26], there were remarkable differences between the measured points in one span of the slab. More importantly, at lower loads, the reinforcement strains of some measured points were larger than 10000 με, but the post-fire slabs had higher carrying capacities (such as Spans B2-PF-A and B3-PF-A). For instance, the reinforcement strains observed were far higher than the yield strains, particularly for Points A (B and C)-S2. The main reason is that the spalling did not occur uniformly, resulting in an inconsistent stress or strain distribution, particularly near the loading plate. On the other hand, the concrete cover basically lost all of its strength, and the stress cannot effectively be transferred between concrete and steel. Thus, the serious bond degradation led to the concentrated or local damage during the residual test. It can be concluded that the conventional reinforcement strain failure criterion (such as 0.01) was not suitable for determining the residual bearing capacity of the post-fire slab; otherwise, the ultimate loads may be seriously underestimated.

5. Theoretical analysis

In this section, several models (flexural and punching shear theories) were used to assess their applicability in the prediction of the residual load capacities of the slabs. The residual properties of concrete and steel were determined based on Ref. [47], as shown in Table 3. In addition, the equivalent concrete residual tensile and compressive strengths across the thickness were calculated according to Ref. [48], and they can be given by

$$f_{cu,T}^{*} = \bar{\varphi}_{c,T} f_{cu,20}, \quad f_{t,T}^{*} = \bar{\varphi}_{t,T} f_{t,20} \tag{1}$$

$$\bar{\varphi}_{c,T} = \frac{\sum_{i=1}^{n} \bar{\varphi}_{c,T_i} \cdot h_i}{h}, \quad \bar{\varphi}_{t,T} = \frac{\sum_{i=1}^{n} \bar{\varphi}_{t,T_i} \cdot h_i}{h} \tag{2}$$

$$\bar{\varphi}_{c,T_i} = 1 - 5.71\times10^{-4} T_i + 6.34\times10^{-7} T_i^2 - 3.42\times10^{-9} T_i^3 + 2.44\times10^{-12} T_i^4 \tag{3}$$

$$\bar{\varphi}_{t,T_i} = 1 - 7.29\times10^{-4} T_i - 1.38\times10^{-6} T_i^2 + 1.18\times10^{-9} T_i^3 - 1.23\times10^{-14} T_i^4 \tag{4}$$

where $\bar{\varphi}_{t,T}$ and $\bar{\varphi}_{c,T}$ are the equivalent residual tensile and compressive strength factor,

444 respectively; $\overline{\varphi}_{c,T_i}$ ($\overline{\varphi}_{t,T_i}$) is the *i*th layer concrete compressive (tensile) strength reduction
445 factor at T_i [45]; T_i is the maximum experienced temperature at *i*th layer; *h* is the slab thickness;
446 h_i is the thickness of *i*th layer; *n* is the number of the layers; $f_{t,T}^*$ and $f_{cu,T}^*$ are the equivalent
447 residual tensile and compressive concrete strength across the section, respectively; $f_{t,20}$ and
448 $f_{cu,20}$ are the tensile and compressive strength at ambient temperature, respectively.

449 ***5.1 Theoretical methods***

450 Theoretical methods included the yield line method [9], membrane action methods [3-4, 7],
451 reinforcement strain difference method [16], and punching shear methods [35, 45-46]. The
452 application of these membrane methods is limited to simply supported slabs at large
453 deflections. Thus, their application or effectiveness is verified by the present fire-damaged
454 continuous slabs subjected to the traveling fires.

455 5.1.1 Bailey method [3-4]

456 Bailey et al. [3-4] proposed a simple analytical method to determine the ultimate load-
457 carrying capacity of two-way concrete slabs incorporating the tensile membrane action. The
458 method was based on rigid-plastic behaviour with a change in geometry; the slab supports the
459 load because of tensile membrane action in the central area of the slab and a ring of
460 compressive membrane action around the perimeter. In this method, four enhancement factors
461 ($e_1 = e_{1m}+e_{1b}$ and $e_2 = e_{2m}+e_{2b}$) for the load carrying capacities caused by the membrane and
462 bending moment were proposed, and the overall enhancement for one slab is given by
463 $e = e_1 - (e_1 - e_2)/(1+2\mu a^2)$, as shown in Table 4. Finally, the deflection failure criterion was used
464 to determine the enhancement factor (*e*) of the slab. Other details can be found in Refs. [3-4].

465 5.1.2 Dong method [7]

466 Dong [7] presented a segment equilibrium method to determine the tensile membrane effects
467 of concrete slabs, as shown in Table 4. This model mainly considers the tensile membrane
468 action that is provided by the vertical component of reinforcement tensile forces after the
469 formation of the mechanism of the plastic hinge line. The deflection failure criterion was
470 proposed to determine the bearing capacity of RC slabs.

5.1.3 Reinforcement strain difference method [16]

The authors [16] proposed the reinforcement strain difference method to predict the residual loads of two-way fire-damaged slabs, as shown in Table 4. In the method, one two-way slab was divided into five parts, i.e., four rigid plates and the central rectangular (square) region. The reinforcement strain difference ($\Delta\bar{\varepsilon}_{sx}$) of a slab is the average reinforcement strain difference between mid-span and the edge of the central rectangular region; it represents the degree of double curvature of the deformed slab. The relationship between the angle of the rigid plates (θ_x) and the reinforcement strain difference ($\Delta\bar{\varepsilon}_{sx}$) was proposed to predict the ultimate loads or load-deflection curve of the slabs. In this study, θ_x and $\Delta\bar{\varepsilon}_{sx}$ are 0.15 and 1.0e-4, respectively.

5.1.4 Punching shear methods

The punching shear methods were given in the Chinese code [35], ACI318-08 code [45] and EN 1994-1-1 code [46], and their equations were summarized in Table 5.

5.2 Theoretical results

The comparison between the theoretical results and the experimental values are indicated in Table 6. For the yield line theory, the ratio (P_y/P_u) ranged from 0.73 to 1.52, with an average value of 1.07 and a variation coefficient of 0.23. Clearly, the predicted ultimate load was not conservative, indicating that the yield line failure mode insufficiently developed in the present tested slabs, due to the strain or stress concentration. As discussed above, for the traveling fire case, the mid-span region of each span was the weakest region due to many original (+) cracks. In contrast, as discussed in Ref. [26], the ultimate load of each span predicted by the yield-line method was smaller than the experimental results. The comparison indicates that the yield line method is not suitable for predicting the ultimate loads of the fire-damaged continuous slabs subjected to the traveling fire, particularly many original cracks appeared in the mid-span region.

As expected, for other methods considering the tensile membrane action, the residual carrying capacities were overestimated. For instance, the average ratios P_b (P_d and P_s) /P_u were 1.36, 1.37, and 1.25, respectively. This conclusion is different from the observation in Ref. [26].

Thus, for the present fire-damaged slabs subjected to traveling fire, the effect of the tensile membrane cannot be considered.

According to the punching shear failure (PSF) mode, the punching shear capacity of each span was predicted by Chinese code [35], ACI 318-08 code [45], and EC4 code [46], as indicated in Table 6. Their average ratios (P_p/P_u) were 0.91 (Chinese code), 0.76 (EN code), and 0.83 (ACI 318-08), respectively. Clearly, compared to the flexural strength, the punching shear capacity of the fire-damaged slab seriously decreased. In addition, this difference is because different relationships between the concrete strength and the punching shear capacity were used in the three current codes, i.e., linear (Chinese code), 1/2 power (ACI 318-08), 1/3 power (EN code). In all, according to Ref. [26] and the present results, it can be concluded that for any fire scenario, the punching shear capacity predicted by ACI 318-08 code was relatively reasonable.

6. Conclusions

This paper presents an experimental investigation on the residual properties of four continuous RC slabs after different compartment fires, and several theoretical methods were used to predict the ultimate load of each span in the present slabs. Meanwhile, the present results were mainly compared with the observation of the previous residual tested slabs subjected to uniform fire. Based on the above investigation, the following conclusions were drawn:

(1) Different from the continuous slabs subjected to the uniform fires, the punching shear failure or the flexural-punching failure mode more easily appeared in the tested slabs subjected to the traveling fires due to many original cross shape cracks in the middle region of each span.

(2) Compared to the fire spread direction and time delay, the reinforcement ratio, reinforcement arrangement and slab’s thickness have more important effects on the residual ultimate loads of the fire-damaged continuous slabs.

(3) Different from the uniform fire case, the yield line method and the tensile membrane action method are not suitable for determining the residual ultimate loads of the

continuous slab subjected to the traveling fire scenario, since the yield line failure mode cannot sufficiently develop due to the strain or stress concentration.

(4) For any fire scenario, the deflection failure criterion (l/50) and ACI 318-08 code can be used to determine the residual ultimate load of the fire-damaged continuous slab with lower span-thickness ratio.

Acknowledgements

This research was supported by the National Natural Science Foundation of China (Grant No. 51408594), the State Key Laboratory for GeoMechanics and Deep Underground Engineering, China University of Mining & Technology/China University of Mining & Technology, Beijing (SKLGDUEK1909). The authors gratefully appreciate this support.

References

[1] L. Lim, C. Wade, Experimental fire tests of two-way concrete slabs, fire engineering research report 02/12, University of Canterbury and BRANZ Ltd, New Zealand, 2002.

[2] L. Lim, A. Buchanan, P. Moss, J.M. Franssen, Numerical modelling of two-way reinforced concrete slabs in fire, Eng. Struct. 26 (2004) 1081-1091.

[3] C.G. Bailey, W.S. Toh, Behaviour of concrete floor slabs at ambient and elevated temperatures, Fire Saf. J. 42 (2007) 425-436.

[4] C.G. Bailey, W.S. Toh, Small-scale concrete slab tests at ambient and elevated temperatures, Eng. Struct. 29 (2007) 2775-2791.

[5] L. Lim, A. Buchanan, P. Moss, J.M. Franssen, Computer modeling of restrained reinforced concrete slabs in fire conditions, J. Struct. Eng-ASCE. 130 (2004) 1964-1971.

[6] L.Z. Li, X. Liu, J.T. Yu, et al., Experimental study on seismic performance of post-fire reinforced concrete frames, Eng. Struct. 179 (2019) 161-173.

[7] Y.L. Dong, C.J. Zhu, Limit load carrying capacity of two-way slabs with two edges clamped and two edges simply supported in fire, J. Struct. Eng-ASCE. 137 (2010) 1182-1192.

[8] Y. Wang, G.L. Yuan, Z.H. Huang, et al, Experimental study on the fire behaviour of reinforced concrete slabs under combined in-plane and out-of-plane loads, Eng. Struct.

128 (2016) 316-332.

[9] Park, R. and Gamble, W.L. Reinforced Concrete Slabs, John Wiley & Sons Inc, Chichester, UK, 2000.

[10] Y. Wang, L A Bisby, T.Y. Wang, et al, Fire behaviour of reinforced concrete slabs under combined biaxial in-plane and out-of-plane loads, Fire Saf. J. 96 (2018) 27-45.

[11] Y. Wang, G.L. Yuan, Z.H. Huang, et al, Modelling of reinforced concrete slabs in fire, Fire Saf. J. 100 (2018) 171-185.

[12] H. Hajiloo, M.F. Green, Post-fire residual properties of GFRP reinforced concrete slabs: A holistic investigation, Compos. Struct. 201 (2018) 398-413.

[13] R. Van Coile, R. Caspeele, L. Taerwe, Reliability-based evaluation of the inherent safety presumptions in common fire safety design, Eng. Struct. 77 (2014) 181-192.

[14] T. Molkens, R. Van Coile, T. Gernay, Assessment of damage and residual load bearing capacity of a concrete slab after fire: Applied reliability-based methodology, Eng. Struct. 150 (2017) 969-985.

[15] C.H. Chung, I.M. Cho Rong, J. Park, Structural test and analysis of RC slab after fire loading, Nucl. Eng. Technol. 45 (2013) 223-236.

[16] Y Wang., W.X. Guo, Z.H. Huang, et al, Analytical model for predicting the load – deflection curve of post-fire reinforced-concrete slab, Fire Saf. J. 101 (2018) 63-83.

[17] J.T. Yu, Experimental and theoretical research on damage assessment of reinforced concrete member after fire, Thesis, Tongji University, Shanghai, 2007 (in Chinese).

[18] X.M. Hou, W.Z. Zheng, Experiment and analysis on the mechanical performance of unbonded prestressed concrete continuous slab after elevated temperature, J. Hunan Univ. 37 (2010) 6-13 (in Chinese).

[19] W.Z. Zheng, X.M. Hou, W.H. Chen, Experiment and analysis on mechanical performance of prestressed concrete simply-supported slab after elevated temperature, J. Harbin Inst. Technol. 43 (2011) 8-13 (in Chinese).

[20] W.Y. Gao, K.X. Hu, J.G. Dai, et al, Repair of fire-damaged RC slabs with basalt fabric-reinforced shotcrete, Constr. Build. Mater. 185 (2018) 79-92.

[21] O. Gooranorimi, G. Claure, F.D. Caso, et al. Post-Fire Behavior of GFRP Bars and

584 GFRP-RC Slabs, J. Mater. Civ. Eng. ASCE 30 (2018) 04017296.
585 [22] C.G. Bailey, I.W. Burgess, R.J. Plank, Analyses of the effects of cooling and fire spread
586 on steel-framed buildings, Fire Saf. J. 26 (1996) 273-293.
587 [23] J.S. Gottfried, G. Rein, Travelling fires for structural design-Part I: literature review, Fire
588 Saf. J. 54 (2012) 74-85.
589 [24] E. Rackauskaite, P. Kotsovinos, A. Jeffers, G. Rein, Structural analysis of multi-storey
590 steel frames exposed to travelling fires and traditional design fires, Eng. Struct. 150(2017)
591 271-287.
592 [25] E. Rackauskaite, P. Kotsovinos, G. Rein, Structural response of a steel-frame building to
593 horizontal and vertical travelling fires in multiple floors, Fire Saf. J. 91 (2017) 542-552.
594 [26] Y Wang, Z.X. Chen, Y.Q Jiang, et al. Residual properties of three-span continuous
595 reinforced concrete slabs subjected to different compartment fires. Eng. Struct, 2020,
596 208: 110352.
597 [27] Y. Wang, Y.K. Duan, Y.J. Zhang, et al, Behaviour of continuous reinforced concrete floor
598 slabs subjected to different compartment fires, Eng. Struct. 197(2019) 109445.
599 [28] G.Q. Li, S.X. Guo, H.S. Zhou, Modeling of membrane action in floor slabs subjected to
600 fire, Eng. Struct. 29 (2007) 880-887.
601 [29] Y.L. Dong, Tensile membrane effects of concrete slabs in fire, Mag. Concr. Res. 62 (2010)
602 497-505.
603 [30] E. Omer, B.A. Izzuddin, A.Y. Elghazouli, Failure of unrestrained lightly reinforced
604 concrete slabs under fire - Part I: analytical models, Eng. Struct. 32 (2010) 2631-2646.
605 [31] E. Omer, B.A. Izzuddin, A.Y. Elghazouli, Failure of unrestrained lightly reinforced
606 concrete slabs under fire - Part II: verification and application, Eng. Struct. 32 (2010)
607 2647-2657.
608 [32] K.A. Cashell, A.Y. Elghazouli, B.A. Izzuddin, Failure assessment of lightly reinforced
609 floor slabs. II: analytical studies, J. Struct. Eng. 137 (2011) 989-1001.
610 [33] B. Herraiz, T. Vogel, Novel design approach for the analysis of laterally unrestrained
611 reinforced-concrete slabs considering membrane action, Eng. Struct. 123 (2016) 313-
612 329.

613 [34] I. Burgess, Yield line plasticity and tensile membrane action in lightly-reinforced
614 rectangular concrete slabs, Eng. Struct. 138 (2017) 195-214.
615 [35] GB 50010-2010 Code for Design of Concrete Structures, China Architecture and
616 Building Press, Beijing, 2010 (in Chinese).
617 [36] Code for fire protection design of buildings (GB 50016-2014). Beijing; 2018 [in
618 Chinese].
619 [37] GB/T 50152-1992 Standard for test method of concrete structures, China Architecture
620 and Building Press, China, Beijing, 1992 (in Chinese).
621 [38] T Gernay. Fire resistance and burnout resistance of reinforced concrete columns. Fire
622 Saf. J., 104(2019) 67-78.
623 [39] T Gernay, J M Franssen. A performance indicator for structures under natural fire. Eng.
624 Struct. 100 (2015) 94-103.
625 [40] J.C. Liu, K.H. Tan, Y. Yao, A new perspective on nature of fire-induced spalling in
626 concrete, Constr. Build. Mater. 184 (2018) 581-590.
627 [41] X.L. An, Fire and Post-fire carrying capacity study of two-way restrained concrete slabs,
628 Thesis, China University of Mining and Technology, 2017 (in Chinese).
629 [42] Antonio Marí, Antoni Cladera, Eva Oller , Jesús M. Bairán. A punching shear mechanical
630 model for reinforced concrete flat slabs with and without shear reinforcement. Eng.
631 Struct. 166 (2018) 413-426.
632 [43] Ala Torabian, Brisid Isufi, Davood Mostofinejad, António Pinho Ramos. Behaviour of
633 thin lightly reinforced flat slabs under concentric loading. Eng. Struct. 196 (2019)
634 109327.
635 [44] Xu Yang, Wan-Yang Gao, Jian-Guo Dai, Zhou-Dao Lu. Shear strengthening of RC
636 beams with FRP grid-reinforced ECC matrix. Compos. Struct. 214 (2020) 112120.
637 [45] ACI Committee 318, Building code requirements for structural concrete and commentary.
638 ACI 318-11, American Concrete Institute, Farmington Hills, 2011.
639 [46] EN 1994-1-1: Design of composite steel and concrete Structures-Part 1-1: General Rules
640 and Rules for Buildings, CEN, Brussels, Belgium, 2007.
641 [47] Wu J. C. Experimental study on fire (post-fire) behaviours of concrete continuous two-

642 way slabs. Thesis, China University of Mining and Technology, China, 2020 (in
643 Chinese).
644 [48] Z.Q. Wang, J. He, Nonlinear analysis of reinforced concrete structures, Harbin Institute
645 of Technology Press, Harbin, 2016 (in Chinese).
646

Figure Captions

Fig. 1. Details of steel reinforcement layouts for the four slabs (all dimensions in mm) (a) Slabs B1, B2 and B3; (b) Slab B4; (c) Typical layout of thermocouples in the concrete slab; and (d) Thermocouples across the full-depth of each slab.

Fig. 2 Details of the test setup (all dimensions in mm): (a) Photograph of the test setup; (b) Photograph of the support; (c) Plan view of the test setup; (d) Cross section 1-1 of test setup.

Fig. 3 Details and instrument layout of four slabs (all dimensions in mm): (a) Layout of reinforcement and concrete strain gages; (b) Layout of displacement transducers.

Fig. 4 Concrete temperature-time curves of the four slabs (the curves with broken line in the figure are the fire curves): (a) Slab B1; (b) Slab B2; (c) Slab B3; and (d) Slab B4.

Fig. 5 Temperature-time curves of the reinforcing steels for the four slabs: (a) Slab B1; (b) Slab B2; (c) Slab B3; and (d) Slab B4.

Fig. 6 Failure modes of Slab B1-PF (all dimensions in mm): (a) Photograph of cracks on the top surface; (b) Crack pattern on the top surface; (c) Photograph of cracks on the bottom surface; and (d) Crack pattern on the bottom surface.

Fig. 7 Failure modes of Slab B2-PF (all dimensions in mm): (a) Photograph of cracks on the top surface; (b) Crack pattern on the top surface; (c) Photograph of cracks on the bottom surface; and (d) Crack pattern on the bottom surface.

Fig. 8 Failure modes of Slab B3-PF (all dimensions in mm): (a) Photograph of cracks on the top surface; (b) Crack pattern on the top surface; (c) Photograph of cracks on the bottom surface; and (d) Crack pattern on the bottom surface.

Fig. 9 Failure modes of Slab B4-PF (all dimensions in mm): (a) Photograph of crack on the top surface; (b) Crack pattern on the top surface; (c) Photograph of cracks on the bottom surface; and (d) Crack pattern on the bottom surface.

Fig. 10 Vertical deflection-load curves of four slabs: (a) Slab B1-PF; (b) Slab B2-PF; (c) Slab B3-PF; and (d) Slab B4-PF.

Fig.11. Ductility factor of absorption energy.

Fig. 12 Horizontal deflection and restraint forces of tested slabs: (a) load-horizontal deflection curves of Slabs B1-PF and B2-PF; (b) restraint force-load curve of Slab B1-PF; and (c) restraint force-load curve of Slab B3-PF.

Fig. 13 Concrete and reinforcement strain-load curves of four slabs: (a) Slab B1-PF; (b) Slab B2-PF; (c) Slab B3-PF: and (d) Slab B4-PF.

Figure

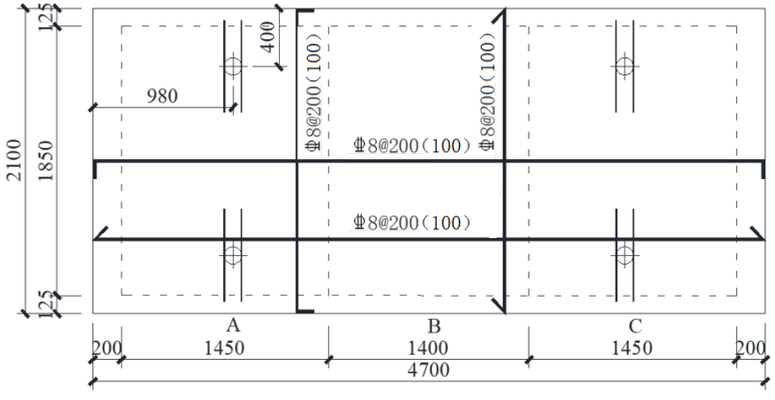

(a) Slabs B1 and B2 (B3)

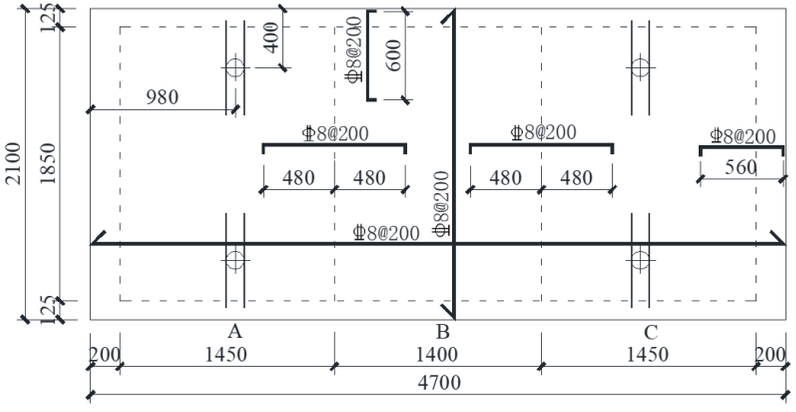

(b) Slab B4

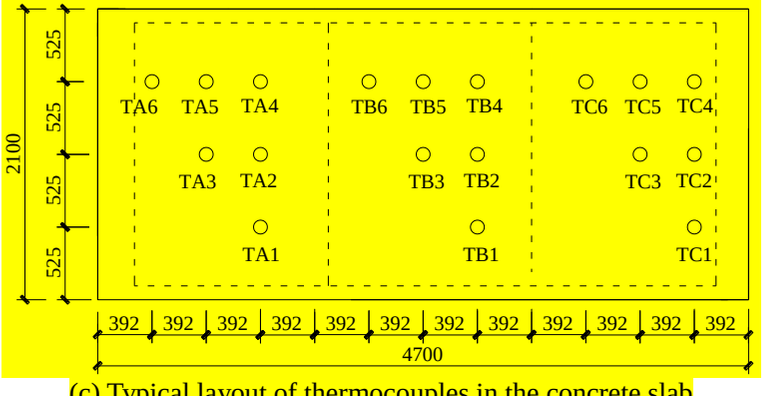

(c) Typical layout of thermocouples in the concrete slab

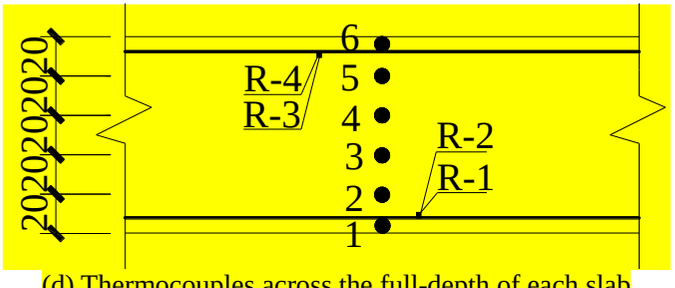

(d) Thermocouples across the full-depth of each slab

Fig. 1. Details of steel reinforcement layouts for the four slabs (all dimensions in mm) (a) Slabs B1, B2 and B3; (b) Slab B4; (c) Typical layout of thermocouples in the concrete slab; and (d) Thermocouples across the full-depth of each slab

(a) Photograph of the test setup

(b) Photograph of the support

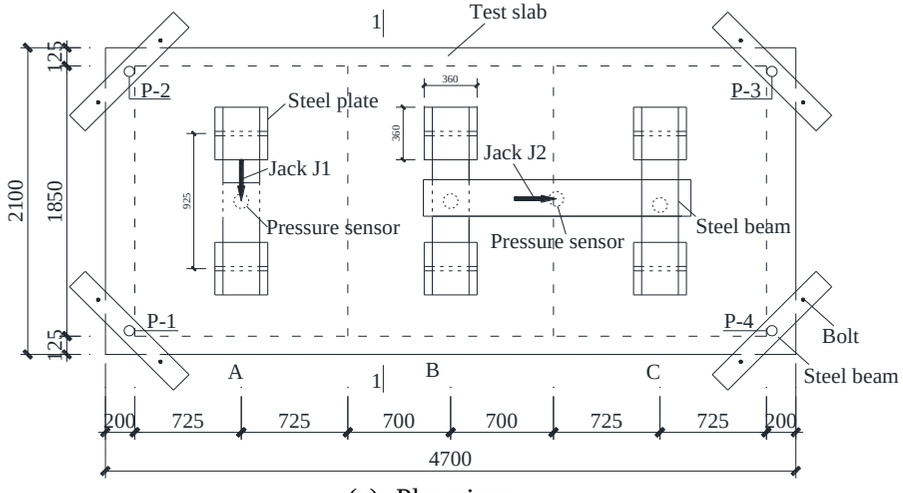

(c) Plan view

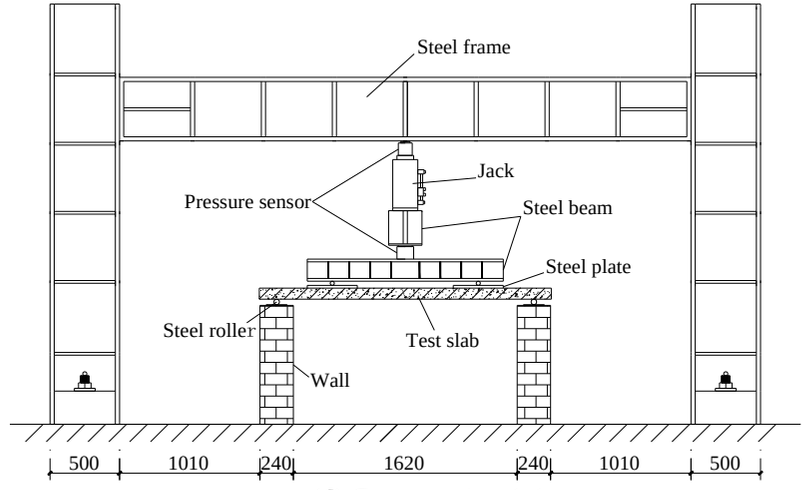

(d) Cross section 1-1

Fig. 2. Details of the test setup (all dimensions in mm): (a) Photograph of the test setup; (b) Photograph of the support; (c) Plan view of the test setup; (d) Cross section 1-1 of test setup

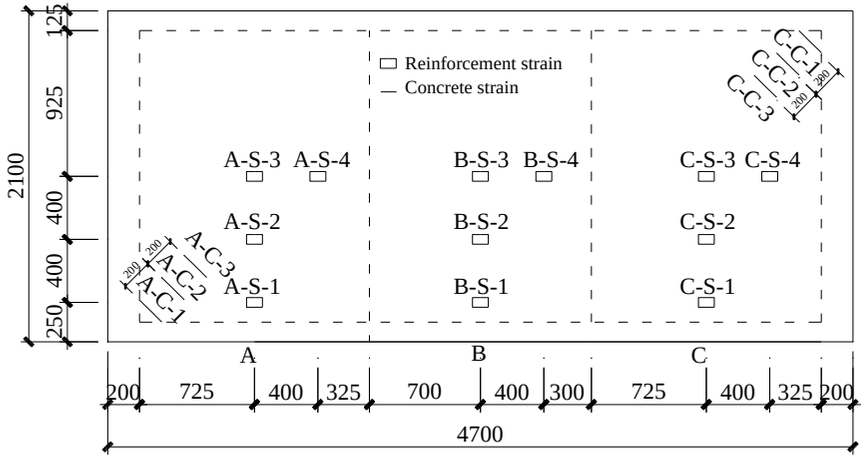

(a) Layout of reinforcement and concrete strain gages

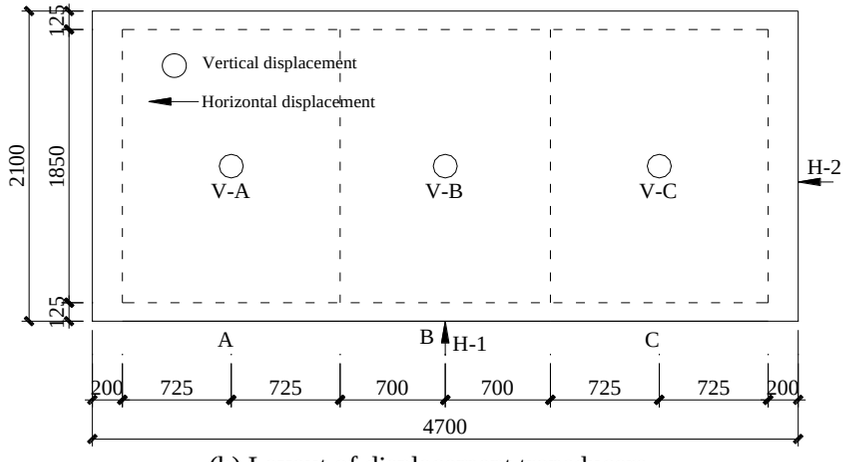

(b) Layout of displacement transducers

Fig. 3. Details and instrument layout of four slabs (all dimensions in mm): (a) Layout of reinforcement and concrete strain gages; (b) Layout of displacement transducers.

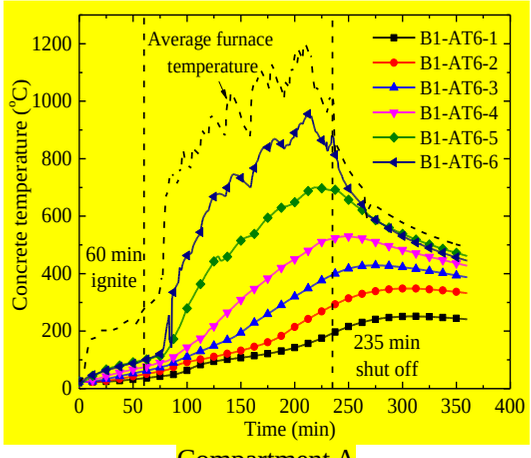

Compartment A

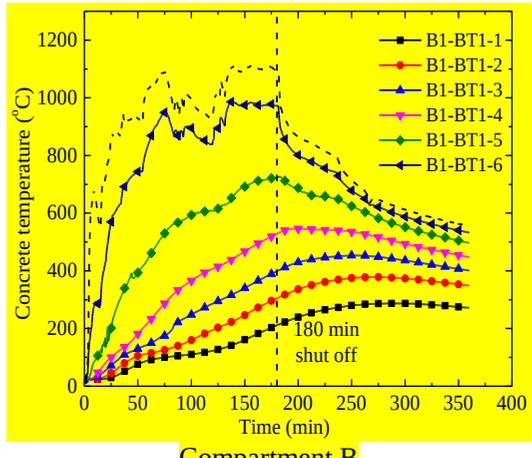

Compartment B

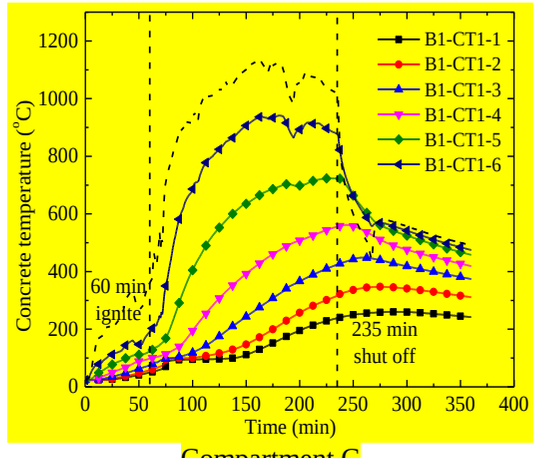

Compartment C

(a) Slab B1

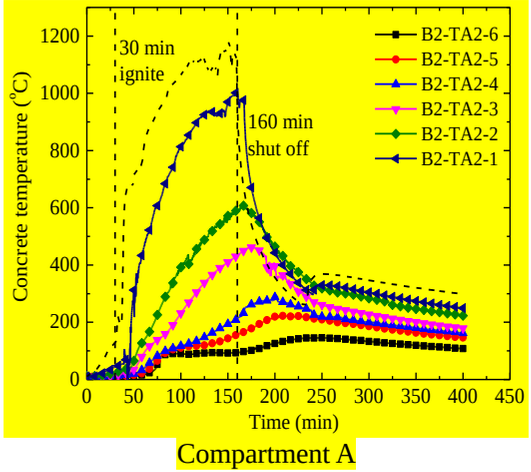

Compartment A

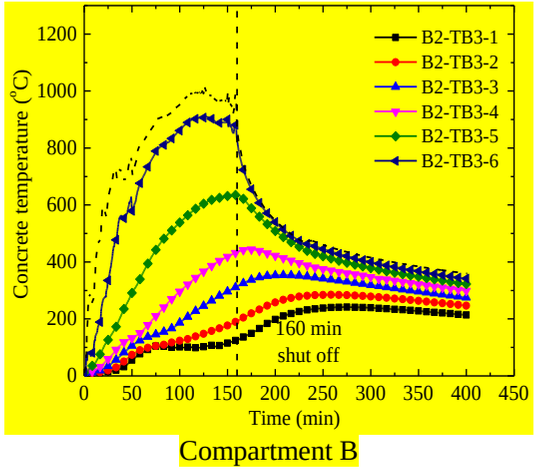

Compartment B

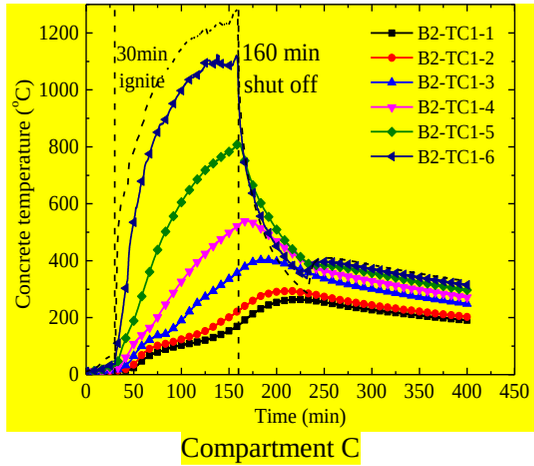

Compartment C

(b) Slab B2

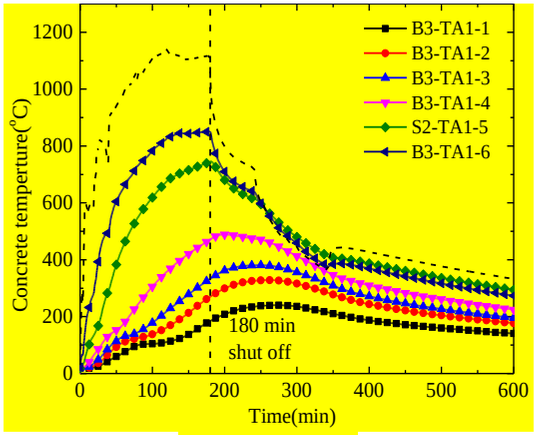

Compartment A

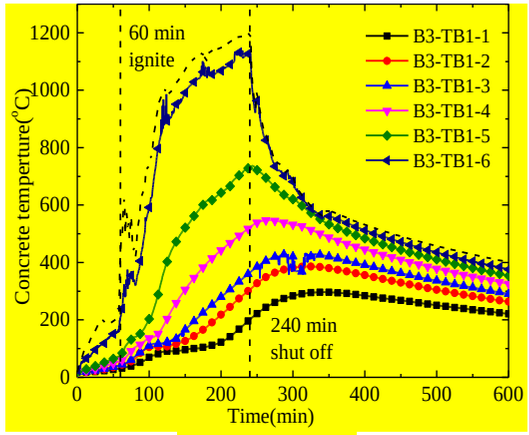

Compartment B

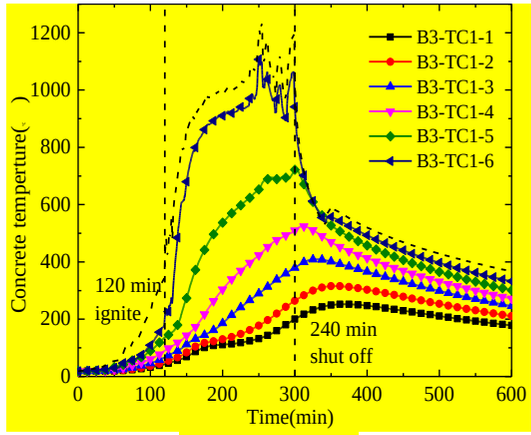

Compartment C

(c) Slab B3

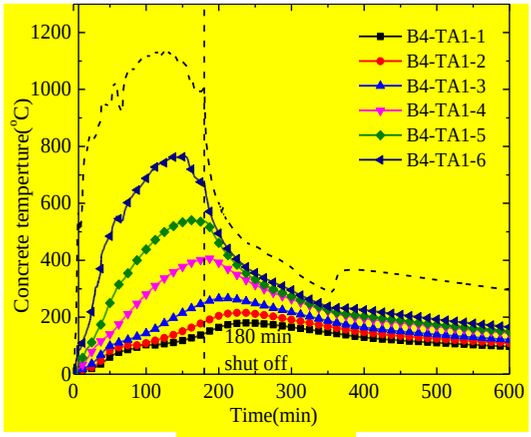

Compartment A

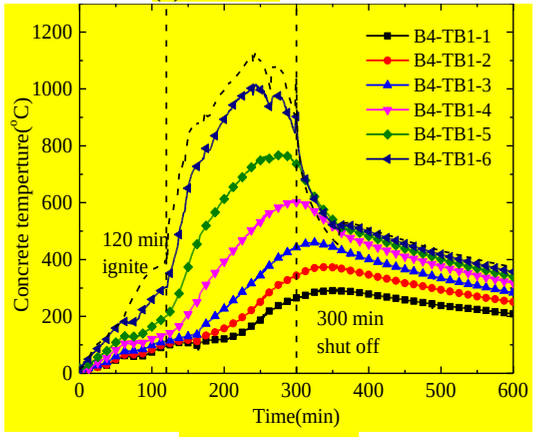

Compartment B

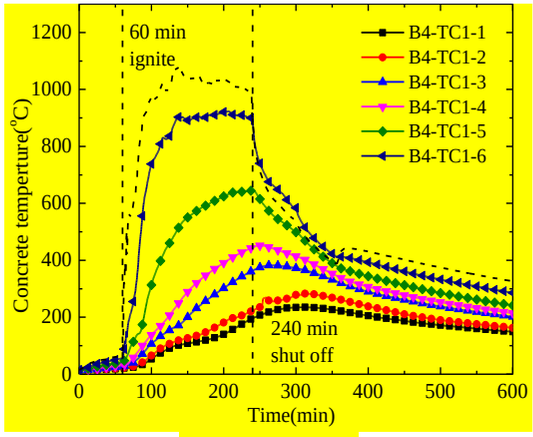

Compartment C

(d) Slab B4

Fig. 4. Concrete temperature-time curves of the four slabs (the curves with broken line in the figure are the fire curves): (a) Slab B1; (b) Slab B2; (c) Slab B3; and (d) Slab B4

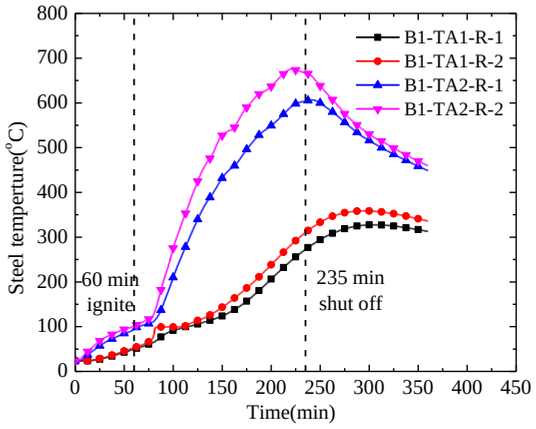

Compartment A

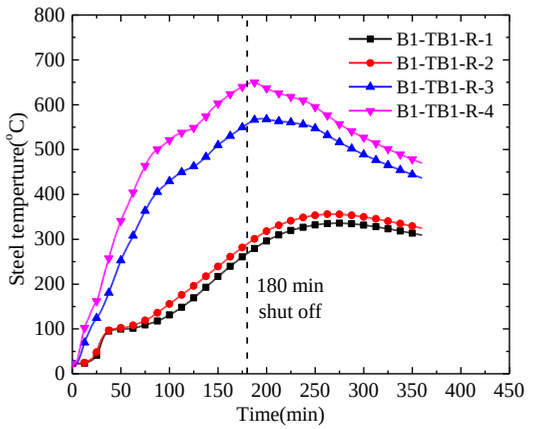

Compartment B

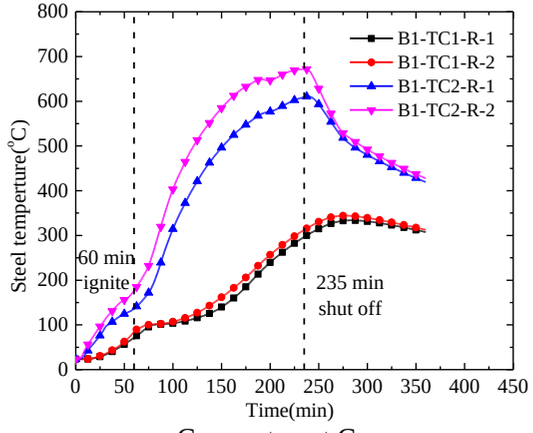

Compartment C

(a) Slab B1

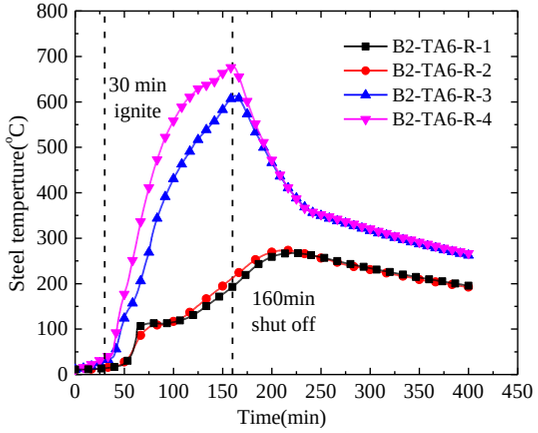

Compartment A

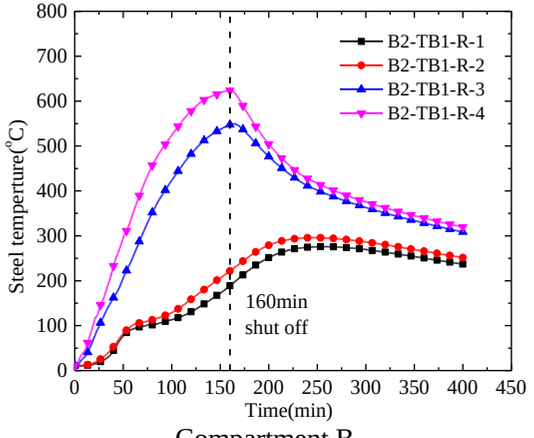

Compartment B

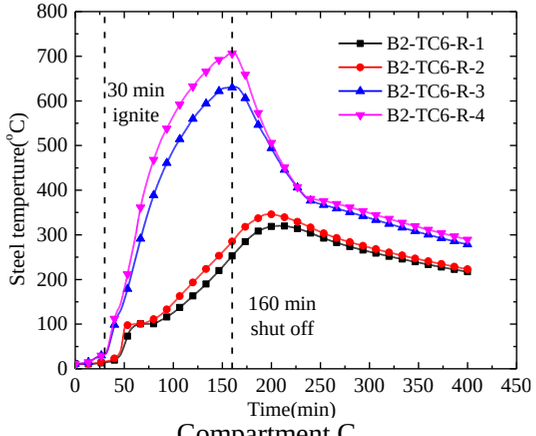

Compartment C

(b) Slab B2

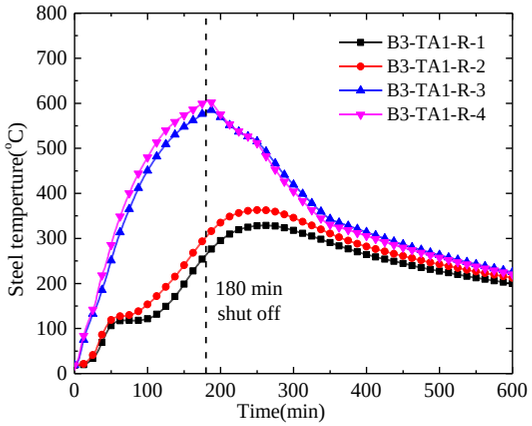

Compartment A

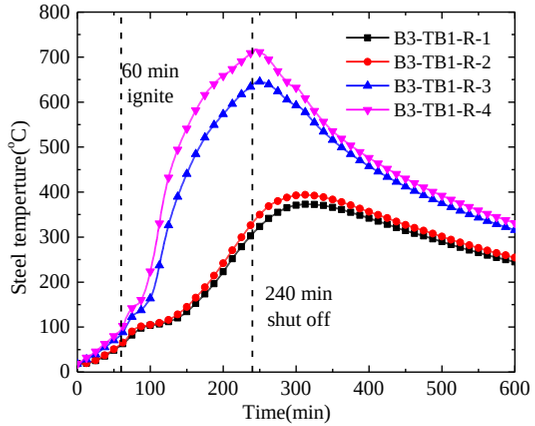

Compartment B

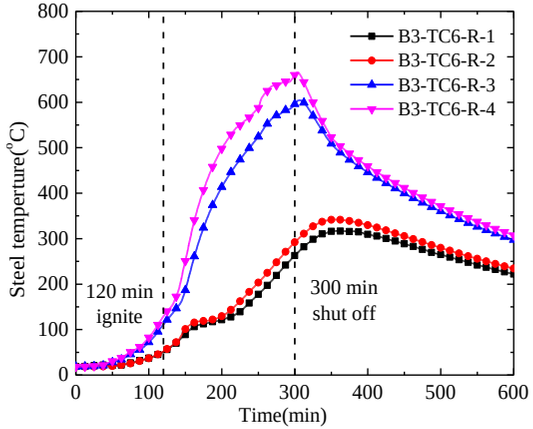

Compartment C

(c) Slab B3

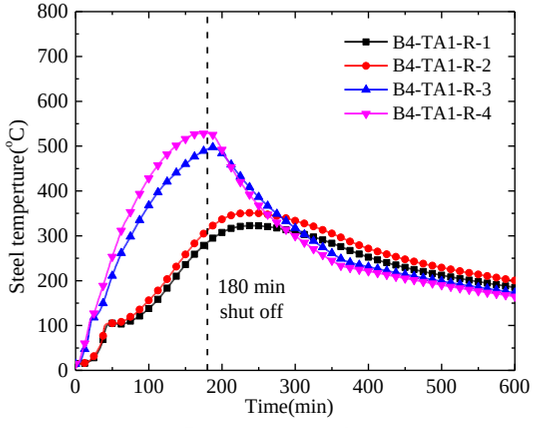

Compartment A

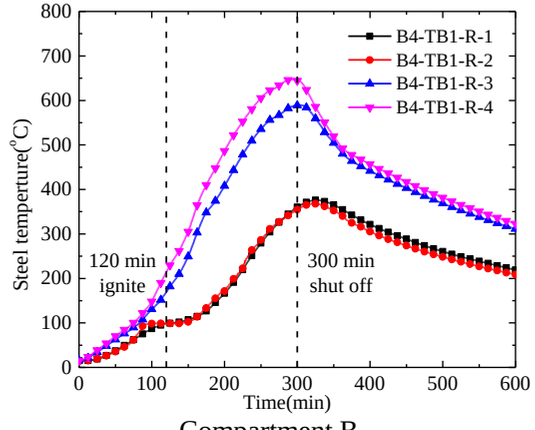

Compartment B

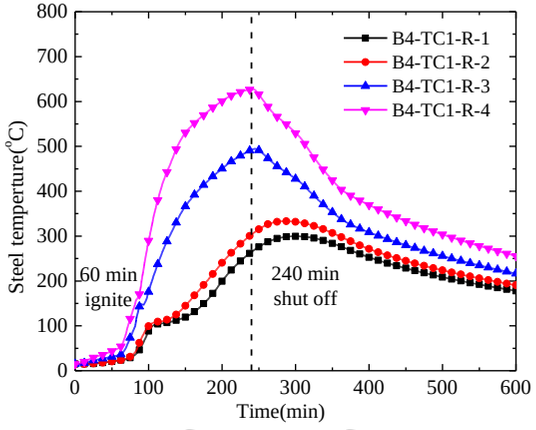

Compartment C

(d) Slab B4

Fig. 5 Temperature-time curves of the reinforcing steels for the four slabs: (a) Slab B1; (b) Slab B2; (c) Slab B3; and (d) Slab B4.

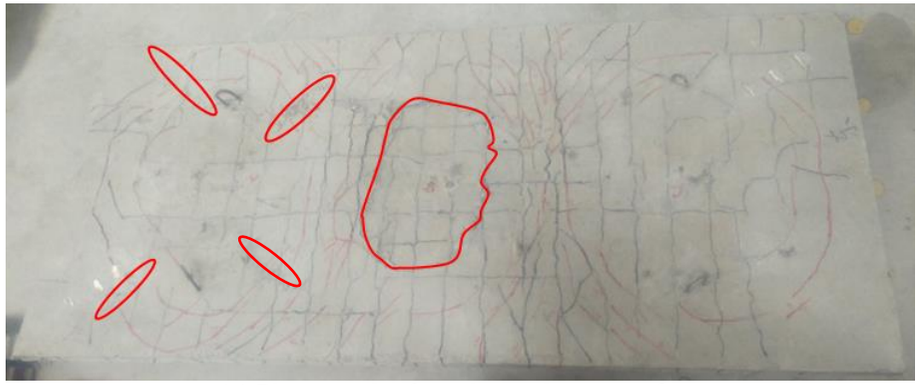

(a) Photograph of cracks on the top surface

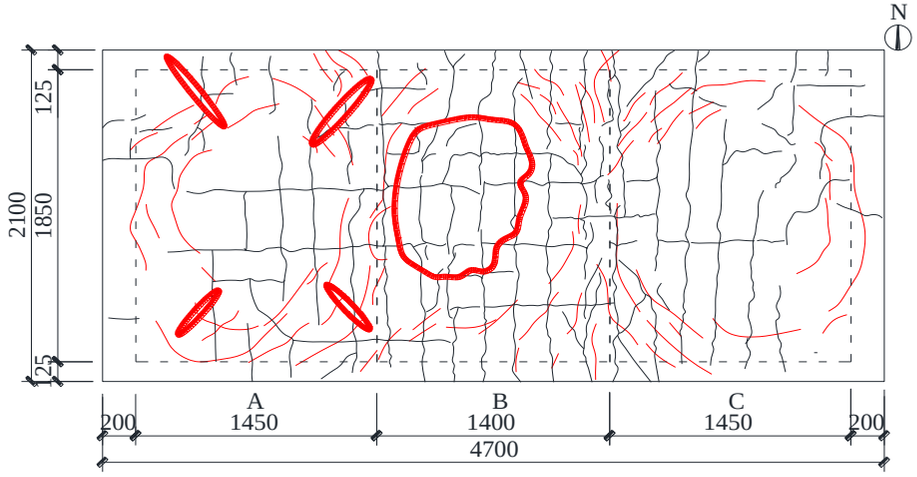

(b) Crack pattern on the top surface

(c) Photograph of cracks on the bottom surface

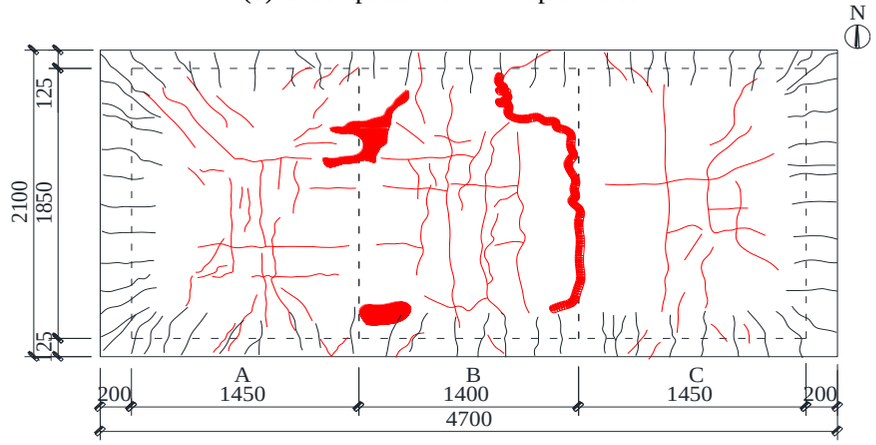

(d) Crack pattern on the bottom surface

Fig. 6 Failure modes of Slab B1-PF (all dimensions in mm): (a) Photograph of cracks on the top surface; (b) Crack pattern on the top surface; (c) Photograph of cracks on the bottom surface; and (d) Crack pattern on the bottom surface

(a) Photograph of cracks on the top surface

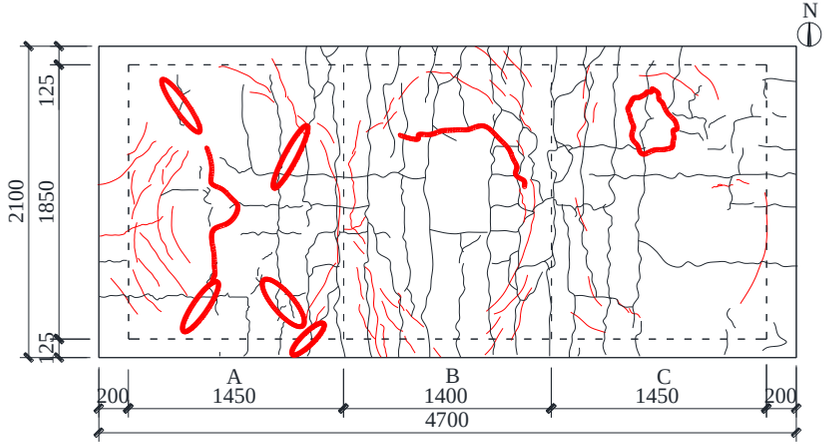

(b) Crack pattern on the top surface

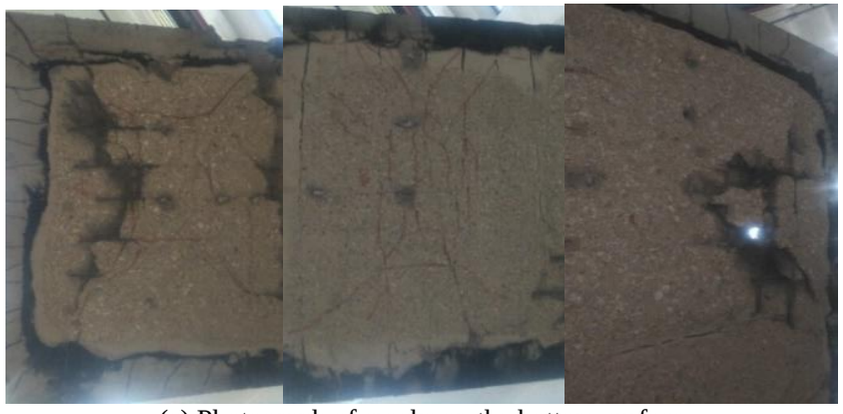

(c) Photograph of cracks on the bottom surface

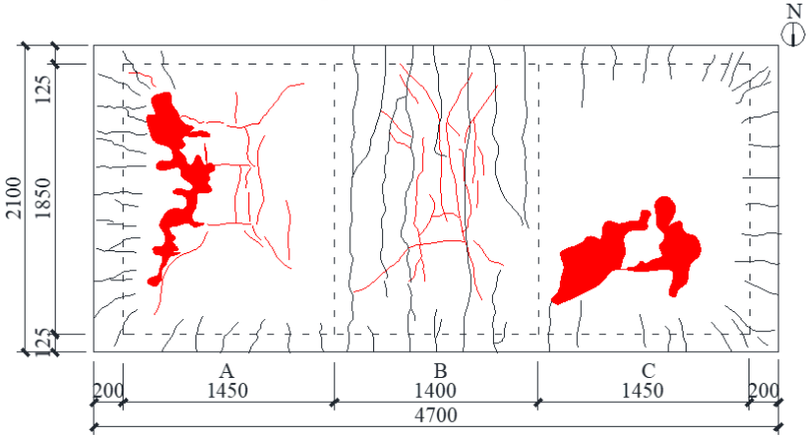

(d) Crack pattern on the bottom surface

Fig. 7 Failure modes of Slab B2-PF (all dimensions in mm): (a) Photograph of cracks on the top surface; (b) Crack pattern on the top surface; (c) Photograph of cracks on the bottom surface; and (d) Crack pattern on the bottom surface

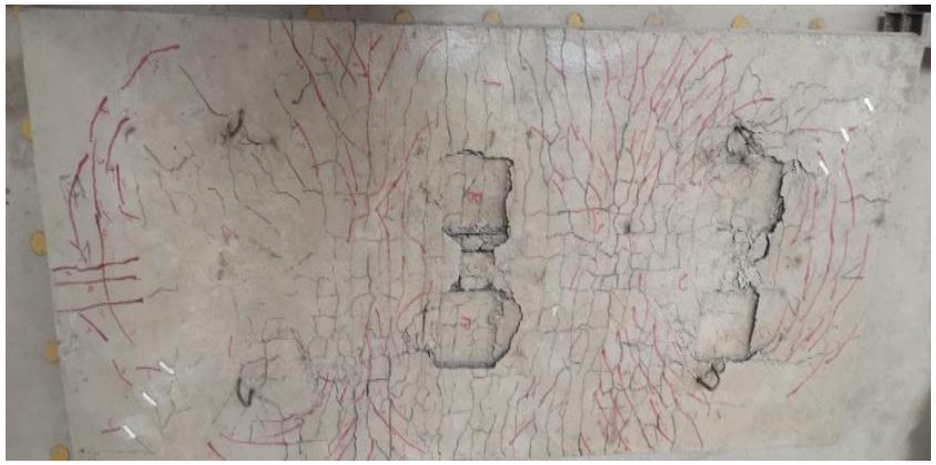

(a) Photograph of cracks on the top surface

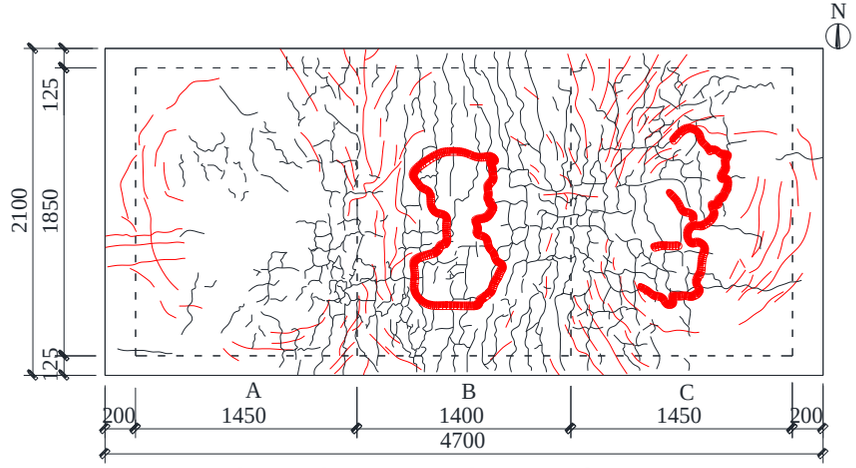

(b) Crack pattern on the top surface

(c) Photograph of cracks on the bottom surface

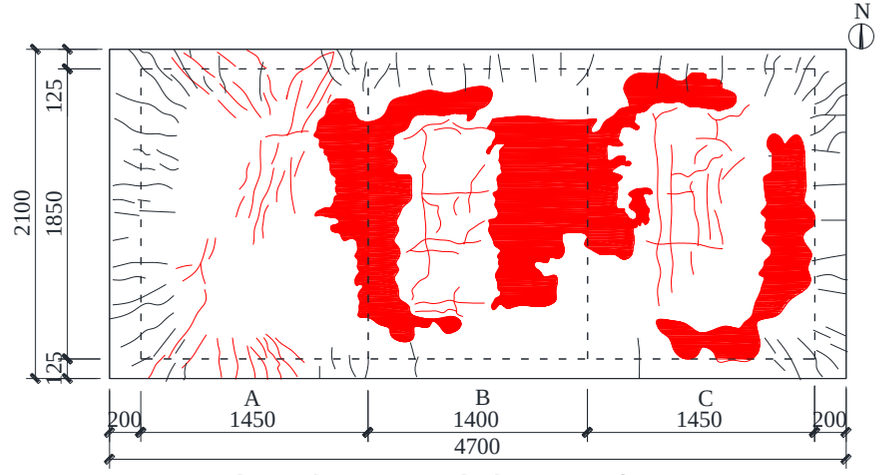

(d) Crack pattern on the bottom surface

Fig. 8 Failure modes of Slab B3-PF (all dimensions in mm): (a) Photograph of cracks on the top surface; (b) Crack pattern on the top surface; (c) Photograph of cracks on the bottom surface; and (d) Crack pattern on the bottom surface

(a) Photograph of cracks on the top surface

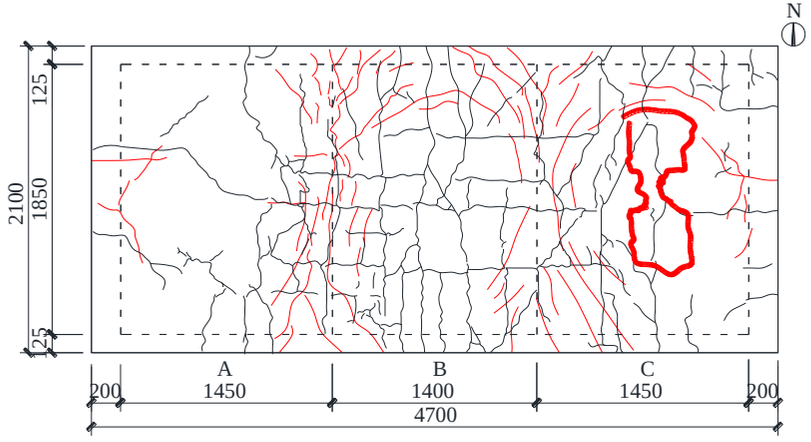

(b) Crack pattern on the top surface

(c) Photograph of cracks on the bottom surface

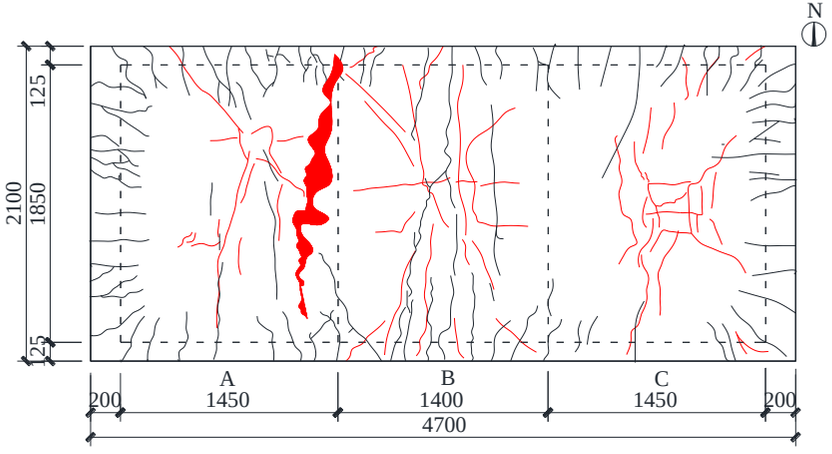

(d) Crack pattern on the bottom surface

Fig. 9 Failure modes of Slab B4-PF (all dimensions in mm): (a) Photograph of crack on the top surface; (b) Crack pattern on the top surface; (c) Photograph of cracks on the bottom surface; and (d) Crack pattern on the bottom surface

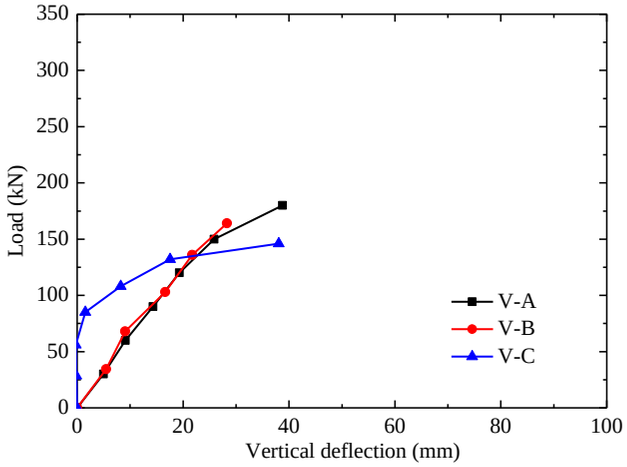

(a) Slab B1-PF

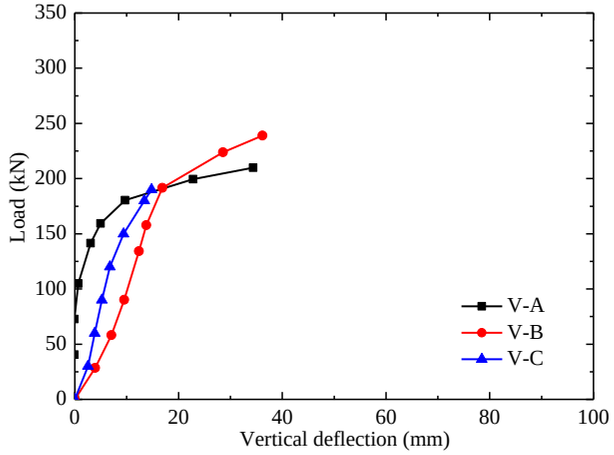

(b) Slab B2-PF

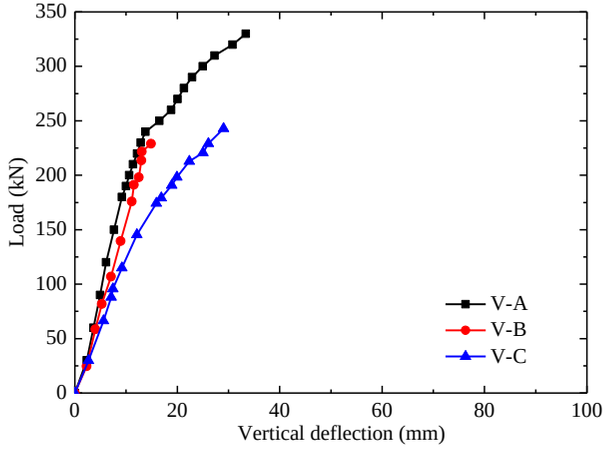

(c) Slab B3-PF

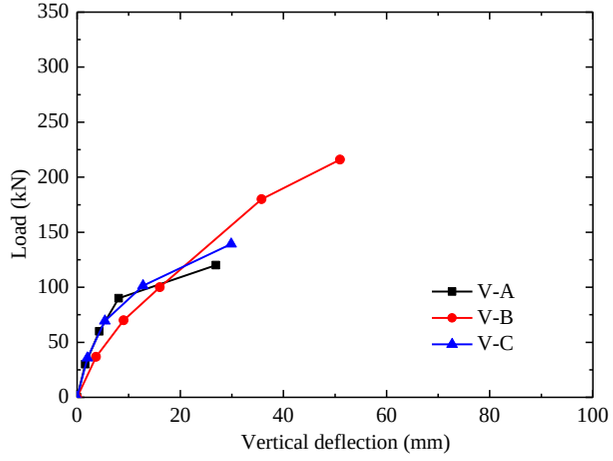

(d) Slab B4-PF

Fig. 10 Vertical deflection-load curves of four slabs: (a) Slab B1-PF; (b) Slab B2-PF; (c) Slab B3-PF; and (d) Slab B4-PF

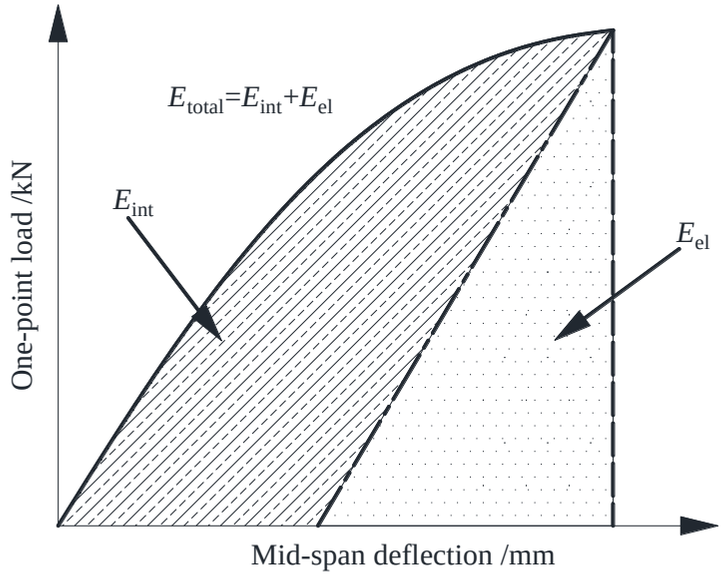

Fig.11. Ductility factor of absorption energy

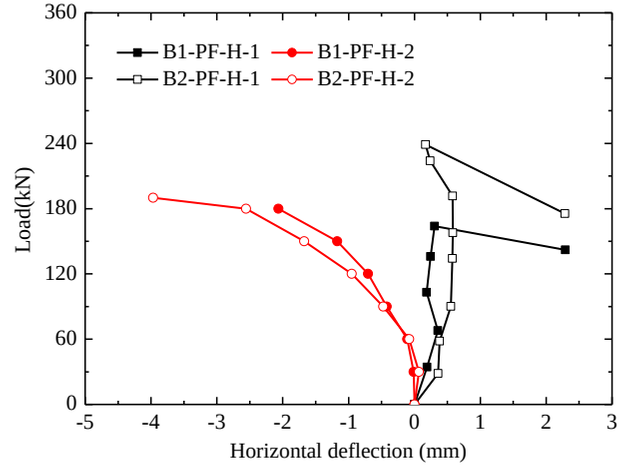

(a) Load-horizontal deflection curves of Slabs B1-PF and B2-PF

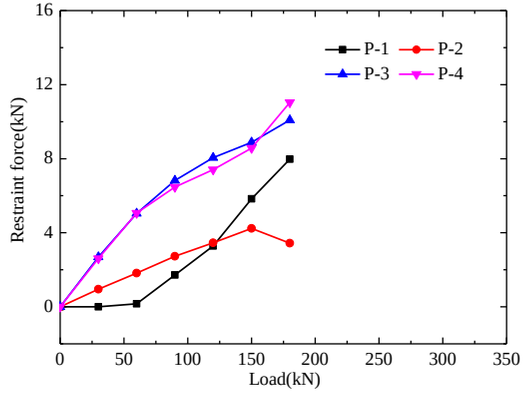

(b) Slab B1-PF

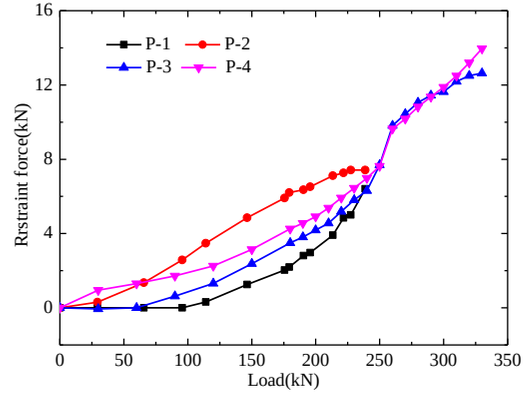

(c) Slab B3-PF

Fig. 12 Horizontal deflection and restraint forces of tested slabs: (a) load-horizontal deflection curves of Slabs B1-PF and B2-PF; (b) restraint force-load curve of Slab B1-PF; and (c) restraint force-load curve of Slab B3-PF.

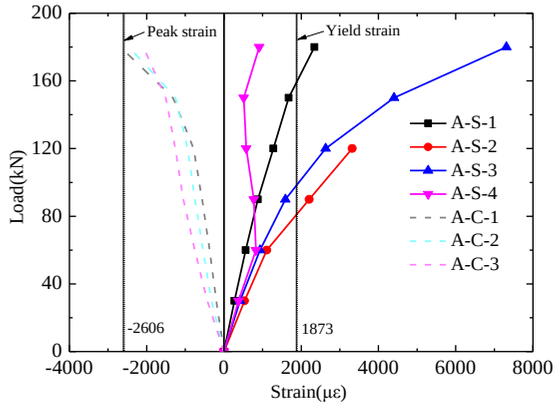

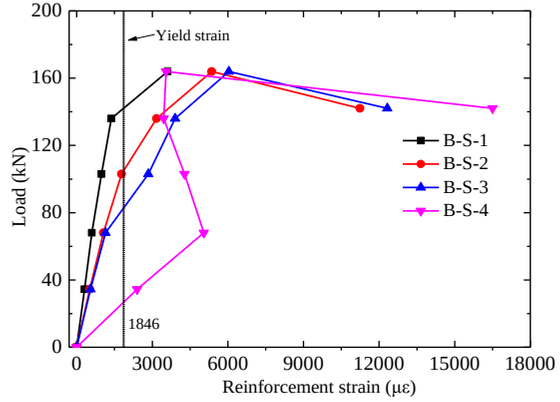

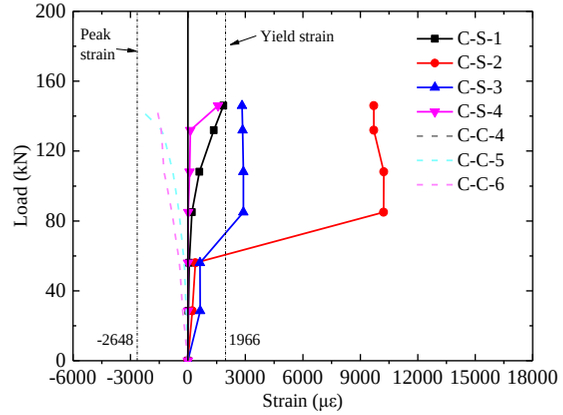

(a) Slab B1-PF

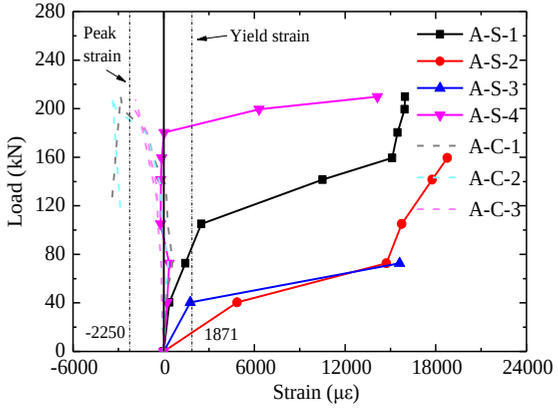

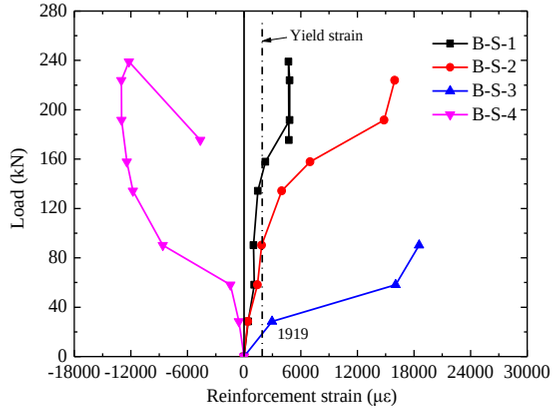

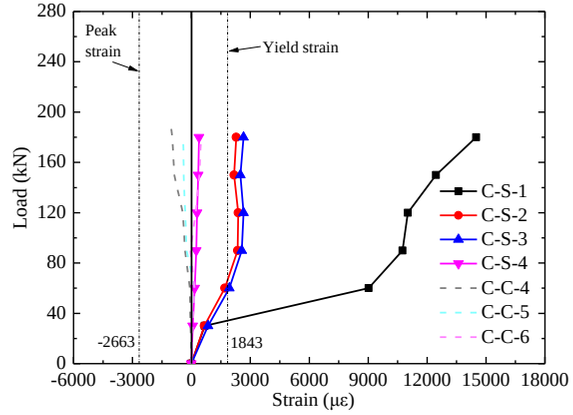

(b) Slab B2-PF

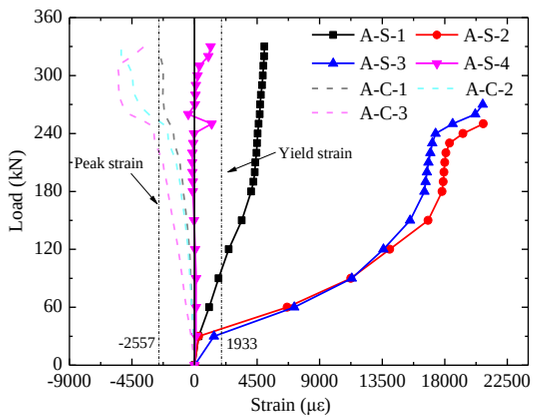

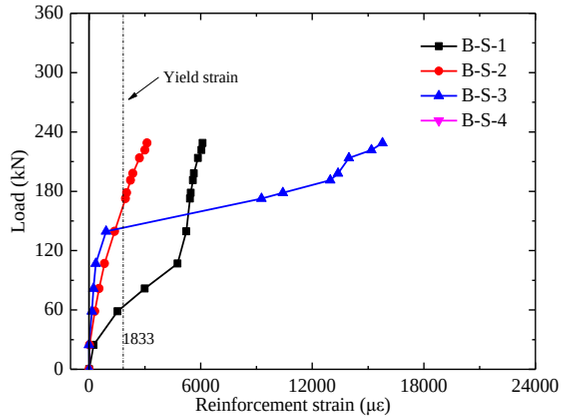

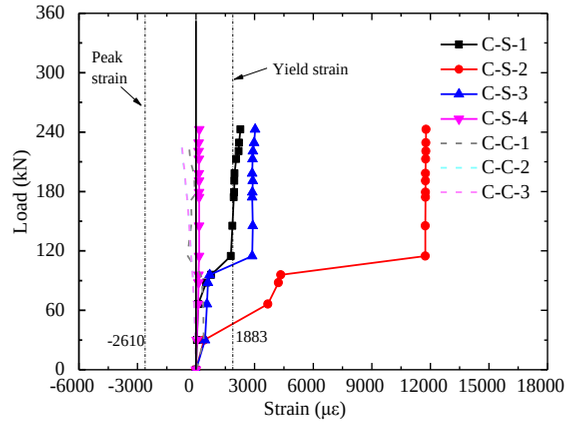

(c) Slab B3-PF

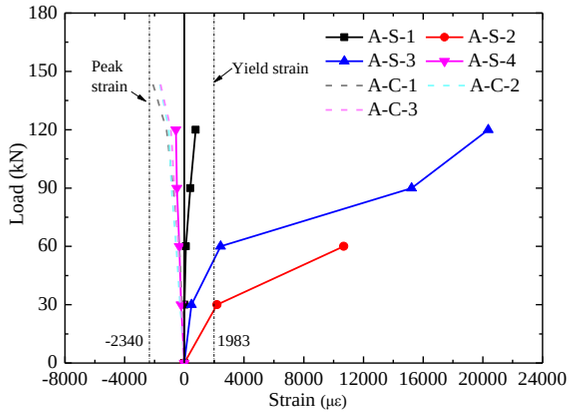

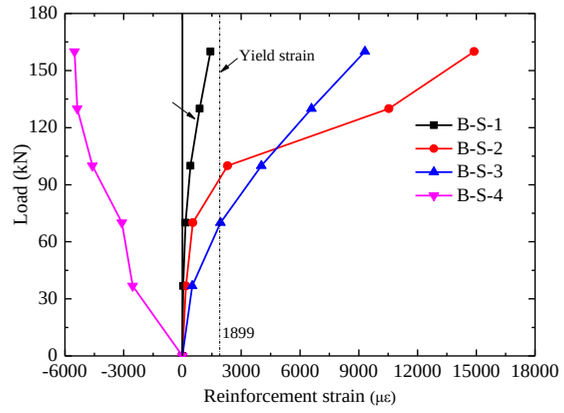

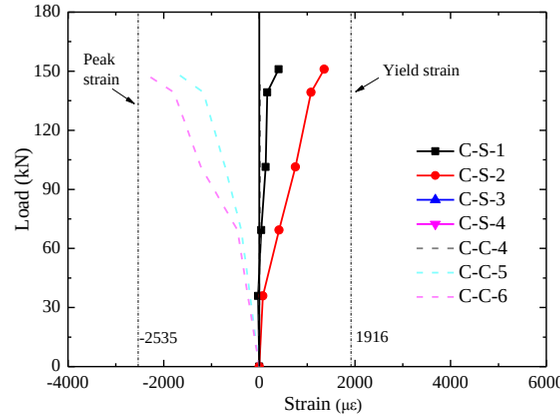

(d) Slab B4-PF

Fig. 13 Concrete and reinforcement strain-load curves of four slabs: (a) Slab B1-PF; (b) Slab B2-PF; (c) Slab B3-PF: and (d) Slab B4-PF

Table

Declaration of interests

x The authors declare that they have no known competing financial interests or personal relationships that could have appeared to influence the work reported in this paper.

☐The authors declare the following financial interests/personal relationships which may be considered as potential competing interests:

Yong Wang: Conceptualization, Methodology, Formal analysis, Investigation, Writing- Original draft preparation.

Yaqiang Jiang: Investigation, Data curation.

Zhaohui Huang: Supervision, Methodology, Writing - Review & Editing

Lingzhi Li: Validation

Yuner Huang: Validation

Yajun Zhang: Formal analysis

Gengyuan Zhang: Validation

Xiaoyue Zhang: Investigation

Yakun Duan: Data curation